FutPrInt50 Academy: Aircraft Design Challenge

Clean-Sheet Design of a Hybrid Electric Aircraft: EGRET Electric Green REgional Transport

C.D. Rotundo
E.E.A. Beyne
K.G. Hildebrandt
Y.K. Peng

Delft University of Technology

TU Delft

FutPrInt50 Academy: Aircraft Design Challenge

Clean-Sheet Design of a Hybrid Electric Aircraft: EGRET Electric Green REgional Transport

by

C.D. Rotundo
E.E.A. Beyne
K.G. Hildebrandt
Y.K. Peng

This research project has received funding from the European Union's Horizon 2020 research and innovation programme under grant agreement No 875551. The findings presented here have been studied, acquired and prepared by the student teams independently. The teams were able to obtain support from the expertise of the FUTPRINT50 Consortium. However, the statements made herein do not necessarily have the consent or agreement of the FUTPRINT50 Consortium. These represent the opinion and investigations of the author(s).

Supervisor:	Dr. ir. T. Sinnige
Institution:	Delft University of Technology
Place:	Faculty of Aerospace Engineering, Delft
Project Duration:	April 14, 2022 - September 2, 2022

TU Delft FUTPRINT50 Academy

Contents

Executive Summary

Air pollution and climate change are important challenges for humanity. Aviation has been perceived as one of the main pollution sources, and climate change propels energy transformation. Thus, to address these challenges, finding a new aircraft configuration for future mobility is the main objective of this project. A regional aircraft, ferrying 50 passengers over a maximum range of 800 km was designed, targeted for entry into service in 2040. Cost and emissions were minimised for a shorter, 400 km mission. A hybrid-electric propulsion system was considered to reduce emissions. The resulting aircraft design is named EGRET, which stands for Electric Green REgional Transport. It was designed and analysed by four Aerospace Engineering M.Sc. students from TU Delft and under Dr. ir. T. Sinnige's supervision.

First, a trade-off was performed at subsystem level, to identify the best options for the propulsion system architecture and energy carrier. The best performing options were combined in three aircraft configurations. These were analysed in a second, aircraft level trade-off. The winner of the trade-off uses series-parallel hybrid propulsion system architecture. The lift of the low wing is augmented by distributed propulsion, which allows a higher wing loading. The energy is provided by SAF.

After the trade-off, preliminary design of the EGRET was started. This was done considering aerodynamics, structures (weight), performance, stability and control, propulsion and power. Most of this was done based on semi-empirical models for conventional aircraft, combined with new or modified analysis tools taking into account aero-propulsive interactions and hybrid-electric propulsion. Minimising total emissions proved hard, the low power density of current battery (assumed 550 Wh/kg) resulted in high battery weights even for low degrees of hybridisation. Therefore, it was decided to instead focus on LTO emissions. To minimise these, the electrical distributed propulsion system provided most of the power near the ground, while in cruise the conventional engines were employed.

The preliminary design of the EGRET was sized over an 800 km mission, including 185 km of diversion and 30 minutes of loiter. This resulted in an MTOM of 24926 kg, and an EOM of 12131 kg. The aircraft cruises at around 5000m, at Mach 0.48, at a lift-to-drag ratio of 18.57. The fuel consumption for the 800 km mission was found to be 2315 kg, and the required electrical energy 732 kWh. A shorter, 400 km mission requires 1567.8 kg of fuel, and 709 kWh. The electrical energy does not differ much from the longer mission, as it is mainly used for take-off and climb. The conventional propulsion system consists of 2 PW127XT, while the distributed propulsion system consists of 10 SPM242-176 electrical motors. LTO emissions consisted of 173.5 kg of CO_2 and 0.47 kg of NO_x for the 400 km mission. Total emissions for that mission were 4940 kg of CO_2 and 19.2 kg of NO_x. A three-view of the aircraft is provided in Appendix A.

1 Introduction

The purpose of this report is to document the technical details and outcomes concerning the research that was performed by the student team from TU Delft through their participation in the *FutPrInt50 Academy Aircraft Design Challenge*. During this project, a hybrid electric aircraft was designed with a primary energy carrier of sustainable aviation fuel (SAF), a secondary energy carrier of batteries, and a series/parallel partial hybrid propulsion system architecture. The designed aircraft features a wing-mounted distributed electric propulsion system with energy carriers connected in series and two conventional wing-mounted turboprops with energy carriers connected in parallel. The aircraft also has a circular fuselage, with a low wing and conventional tail configuration. Throughout the course of this project, the following top-level aircraft requirements (TLARs) have been maintained.

Table 1.1: A list of top-level aircraft requirements that have been maintained throughout the course of the project.

TLAR	Value
Number of passengers	50
Passneger weight	106 kg per passenger (5300 kg total)
Design range	800 km
Maximum Design cruise speed	Mach 0.48
Maximum payload	5800 kg
Reserve fuel policy	185 km + 30 minutes holding
Minimum Rate of Climb (MTOM, SL, ISA)	1850 ft/min (9.398 m/s)
Maximum time required to climb to FL 170	13 minutes
Maximum operating altitude	7620 m (25000 ft)
Maximum take-off field length	1000 m
Maximum landing field length	1000 m
Benchmark for DOCs	Design W_{PL} with 400 km mission

The development of the aircraft proceeded as follows. First, a subsystem trade-off was performed to identify subsystems that would be used in the design concepts under consideration for this project. This included determining a suitable propulsion system architecture and primary energy carrier based on qualitative information obtained from the available literature and according to the authors' opinions. After completing the subsystem trade-off, an aircraft-level trade-off was performed, where three aircraft concepts that the authors considered to be feasible were analyzed and compared both qualitatively and quantitatively. The concept selected from this trade-off was then held fixed and developed further to satisfy the TLARs. During the technical implementation, a constraint analysis was first performed to obtain the wing and power loading requirements for the aircraft, and then more detailed subsystem-level analyses were completed to motivate the design decisions that were made. After obtaining all geometric parameters for the design, preliminary three-view drawings of the aircraft were produced and all findings were assessed to ensure that the TLARs are satisfied by the designed aircraft.

During the subsystem-level design and analysis aspects of the project, low-fidelity analyses were performed to refine the design of the aircraft concept and to determine its aerodynamic performance (in Section 3.3), stability and control characteristics (in Section 3.4), propulsion system characteristics (in Section 3.5), mass properties (in Section 3.6), and overall performance (in Section 3.7).

The primary goals for this project were to design an aircraft with reduced emissions especially within close-proximity to the airport to decrease the environmental impact of flying.

2
Determining the Aircraft Concept

The configuration of the hybrid-electric aircraft was first divided into subsystems, where a trade-off at subsystem level was completed. Thereafter, three aircraft configurations were determined based on the outcome of this trade-off. The three concepts combine some of the best systems from the subsystem trade-off to prevent unfeasible combinations of subsystems and to exploit synergies. Hereafter, a secondary trade-off was determined in order to determine the final configuration of the aircraft.

2.1. Subsystem Trade-off

The subsystem trade-off was completed for the propulsion system architecture and type of primary energy carrier. To complete this trade-off, a list of criteria was established and weights were assigned by the authors to the different criterion based on engineering judgment of their relative importance. The criteria and their corresponding weights are found in Table 2.1.

Table 2.1: A list of criteria that was applied to the subsystem trade-off.

Criterion	Weight	Description
Complexity	4	Relative complexity that is introduced into the design
Cost	3	A score of the relative cost (a high score indicates low costs)
Operations	3	The predicted amount of airport operational changes required
Safety	4	A metric to quantify potential safety concerns introduced
Sustainability	5	A metric to penalize concepts associated with high emissions
Technology Readiness	5	The likelihood for the system to be implemented by 2040
Weight	5	The relative potential to minimize additional weight

A review of the available literature regarding each of the relevant subsystems is provided within the following sections of this chapter. The literature study performed for each section was used to motivate the score that was assigned to each configuration under consideration during this project.

2.1.1. Propulsion System Architecture

The outcome of the propulsion system architecture trade-off is presented in Table 2.2. The series architecture is the best choice when considering the trade-off criteria, followed by the parallel architecture, and thereafter the series/parallel and turbo-electric architectures.

Table 2.2: Propulsion system architecture trade-off scores

Configuration	Complexity	Cost	Operations	Safety	Sustainability	Weight	Technology Readiness	Total
Series/Parallel	3	4	4	5	4	5	3	116
Series	4	4	4	3	5	4	3	112
Parallel	3	4	4	4	4	4	3	107
Turboelectric	5	5	5	3	2	4	2	102

In terms of complexity, the turbo-electric scored the highest because it does not require batteries to store energy and deliver power. The remaining options are more complex as they all require batteries. The

parallel architecture has a mechanical coupling between the electric motors and engine, thus making it more complex than the series architecture [29]. The series/parallel features this same mechanical coupling and therefore receives the same score as the parallel architecture.

Because the turbo-electric architecture does not require large batteries, it is expected that the costs associated with the electric powertrain would be lowest for this architecture. This is why this architecture has earned the highest score for cost. The remaining options were assigned a score of 4 for cost due to the requirement for additional measures required to support the entire life-cycle of the batteries.

A score of 5 is awarded for the operations of the turbo-electric architecture as no charging of the batteries are required due to the fact that the electrical system is driven directly by an engine inside the aircraft. The other three architectures most likely require batteries to be charged or replaced at the airport, requiring new airport infrastructure. Thus these concepts received a score of 4 for operations.

The turbo-electric has no risk of battery fire, though if the turbine or electrical system fails, the aircraft loses thrust immediately. This is why it has received a score of 3 for safety. The series architecture also received the same score due to the fire hazard caused by the batteries and the fact that an electrical system malfunction would lead to a total loss of thrust. While the parallel architecture still presents the battery fire hazard, the aircraft would be able to fly in case of an electric system failure, awarding it a 4 for safety. The series/parallel architecture is also at risk of a fire hazard due to its batteries. However, the combination of different architectures will lead to a higher level of redundancy, as if capabilities to deliver power from one of the two energy sources or groups of propulsors is lost, then all power is still not lost. This is why it has also been awarded a score of 5 for safety.

Concerning sustainability, the turbo-electric architecture has been awarded a 2. This is because the engine still needs to provide peak power, meaning that it would be quite heavy and it would require a large rated power, leading to an increased fuel consumption. The series architecture has been awarded a 5 because the turbine can be operated at its most efficient point throughout the mission, leading to possibly a relatively low energy consumption. The parallel architecture received a 4 for sustainability because it is less efficient than the series architecture at current technology levels. However, due to the lower weight of the powertrain, the fuel consumption is lower [29]. The series/parallel architecture was also awarded a 4 because of its relatively easy change of topology during operations. This could ensure that the aircraft is always operating at a point of high efficiency, and periods of relatively high fuel consumption could be restricted to designated segments of the overall mission profile. Nonetheless, it may be possible that the high weight of this architecture would counteract this supposed benefit [29].

The turbo-electric, series and parallel architectures all received a score of 4 for weight when analysing the architectures at a subsystem level. The simple architecture of the turbo-electric allows the batteries to be lighter, though its engine will be heavy as it must be sized for peak power. The series architecture will also be heavy due to the large electric motors that are required, leading to a large powertrain weight. For the parallel architecture, the gas turbine may be smaller as it does not need to provide peak power on its own. However, the required mechanical coupling adds weight. The series/parallel architecture was given the highest score in terms of weight despite its need for both a mechanical coupling and separate engines. This is because it may be possible to reduce the overall mass of the propulsion system by combining the series and parallel architectures, and leveraging strategic power delivery options. At this stage, it was difficult to directly quantify the effects of weight due to the propulsion system architecture and thus it was considered more favourable to reward the most general option.

In terms of technology readiness, turbo-electric has been used in the propulsion systems of ships and trains. Moreover, due to its simplicity and lack of battery requirements, it is anticipated that implementing this technology may be relatively straight-forward. The major downside with this technology that it may only ever yield a lower fuel consumption and be profitable to airliners if it features correct implementations of next-generation technologies such as distributed electric propulsion with boundary layer ingestion and energy-harvesting capabilities, or alternative fuels [16]. Currently, it has not been found to be more fuel-efficient on its own. This dependence on other configuration-specific technological advancements precludes its use in general aviation, especially for a clean-sheet design. Therefore, it has been awarded a score of 2. The series architecture has not yet been tested for flight, although several demonstrators are under development. The main drawback of this technology is its dependence on batteries, which currently do not have a high enough specific energy to make this system feasible.

This applies to the parallel and series/parallel configurations. These three architectures are still under development remain to be successfully proven [29]. The series/parallel configuration has the advantage of being the mot generalized, and thus it may act as a turboelectric, series, or parallel at differing mission segments. This increases its potential, as the size of the batteries could be reduced through the application of strategic power delivery schedules. It was nonetheless assigned a score of 3, along with the series and parallel architectures, as these potential benefits remain to be exploited.

2.1.2. Primary Energy Carrier

For the primary energy carrier, three options were investigated: sustainable aviation fuel (SAF), hydrogen and ammonia. The trade-off results are presented in Table 2.3. As can be seen, SAF by far received the best score, with hydrogen as second, and ammonia being assigned the lowest score.

Table 2.3: Primary energy carrier trade-off scores

Configuration	Complexity	Cost	Operations	Safety	Sustainability	Weight	Technology Readiness	Total
Sustainable aviation fuel (SAF)	5	3	5	5	2	5	5	124
Hydrogen	3	4	3	2	4	4	3	96
Ammonia	4	5	3	2	4	3	2	93

SAF largely resembles kerosene in its chemical structure and can straightforwardly replace kerosene. This means that the same fuel tanks, engines and refuelling practices can be utilised with this fuel [35]. Engine manufacturers have also begun converting their current engines to being 100% compatible with SAF. Moreover, some airliners are already using SAF, and it does not add any considerable weight to the aircraft due to its resemblance to kerosene. SAF can also be considered equally as safe as kerosene due to its similar chemical structure. This is why SAF has been awarded a 5 for complexity, operations, safety, weight, and technology readiness. However, SAF is generally quite expensive and in short supply. In 2020, it costs more than double the price of kerosene [34], which is why it has received a score of 3 for cost. While SAF overall may decrease the emissions by closing the carbon loop, greenhouse gases are still emitted due to its chemical formula [35]. SAF has been assigned a score of 3 for sustainability, which is the lowest score of the three options under consideration.

Using hydrogen as a fuel requires complex cryogenic tanks and new types of engines, which is why it has been awarded a 3 for complexity. In terms of cost, using liquid hydrogen for short-haul applications would only result in an approximate increase of $5–$10 in passengers costs by the year 2035 [49], thus causing it to receive a score of 4 for costs. Airports would require new infrastructure in place and new maintenance routines with hydrogen, thus causing it to receive a score of 3 for operations. Moreover, hydrogen has only been awarded a 2 for safety due to its high flammability and the high pressures that it must be stored at. However, hydrogen scores high in terms of sustainability because no carbon dioxide or nitrogen oxides are produced while burning this fuel. Nonetheless, only green hydrogen is not directly associated with any emissions during its production, and somewhat considerable carbon emissions are associated with the much cheaper alternatives of blue or gray hydrogen. Therefore, hydrogen has been given a score of 4 for sustainability. Using hydrogen may require the aircraft to be heavier despite its high gravimetric specific energy. This is due to its low density, which results in a low volumetric specific energy, meaning that the hydrogen would need to be stored in relatively large tanks, thus resulting in an increase in weight of both the airframe and fuel tanks. Hydrogen has therefore been assigned a value of 4 for weight. Lastly, hydrogen has been awarded a score of 3 for technology readiness because it does not appear that current major turboprop manufacturers are investing relatively significant portions of their business activities towards the development of hydrogen-powered technologies in comparison. Nonetheless, a notable amount of work has been started concerning the development of liquid or gaseous hydrogen powered aircraft in both industry and academia.

Using ammonia as an alternative fuel does not require significant engine design changes, if using it as a combustion fuel [4]. This gives ammonia a score of 4 for complexity. Moreover, ammonia is predicted to be able to complete with the cost of conventional jet fuels, giving it a score of 5 for cost [47]. On the other hand, like with hydrogen, new infrastructures and maintenance practices would need to be established for airliners to consider using ammonia-powered aircraft, thus causing it to receive a score of 3 for operations. In terms of safety, ammonia is toxic, corrosive and can be highly flammable, which

is why it has been awarded a score of 2 for safety [42]. For sustainability, ammonia has been awarded a 4. While it does not emit carbon dioxide, nitrogen oxides will be emitted due to its chemical formula. In terms of weight, ammonia has a low gravimetric energy density compared to hydrogen and SAF, indicating that a high volume would need to be taken on board, increasing the overall weight of the aircraft. Lastly, ammonia has been awarded a 2 for technology readiness because of its more recent consideration, and because proof of concepts must still be produced.

2.2. Aircraft Level Trade-off

The subsystems with the highest ranking from the subsystem trade-off were combined into three aircraft configurations. A second trade-off, at aircraft level, was then performed to find the final aircraft configuration. The aircraft level trade-off combines some of the best subsystems into different configurations in order to prevent infeasible combinations of subsystems and to exploit synergies. The trade-off criteria, along with their respective weights and descriptions are presented in Table 2.4.

Table 2.4: A list of criteria that was applied to the aircraft level trade-off.

Criterion	Weight	Description
Cost	2	The total cost associated with the aircraft, which impacts its appeal to aircraft manufacturing companies and airlines
Operations	3	The aircraft shall be able to use existing airport infrastructure and existing operational procedures as much as possible
Sustainability	5	The aircraft shall minimise emissions to mitigate the environmental impact of flying
Technology Readiness	4	Likelihood for technology used in aircraft configuration to be ready by 2040
Weight	5	The relative potential to minimize additional weight

In total, three configurations were created. These are summarised in Table 2.5. It was decided that all configurations would be using SAF as the primary energy carrier as it adds the least amount of weight to the design, as seen in Table 2.3. This is desirable when considering a hybrid-electric aircraft as the batteries may be considerably heavy. Moreover, current aircraft technologies and infrastructures may be used with SAF, which guarantees a higher success of entry into service by 2040, both in terms of ensuring that the aircraft is certified on-time and for airports to be able to allow the aircraft to operate on the ground without any major changes. Of course, the batteries must be charged and/or replaced periodically, although this does not require an entirely new refuelling system, as additional measures would only need to be added to the already well-established systems that are currently in-place.

Table 2.5: Aircraft configurations for secondary trade-off analysis

Configuration 1	A high wing aircraft, with a t-tail, and a series propulsion system combined with a distributed propulsion system integration. The primary energy carrier is SAF and the secondary energy carrier is batteries. The supplied power ratio is 0.2 and the shaft power ratio is 1.0.
Configuration 2	A low wing aircraft, with a conventional tail, and a series/parallel propulsion system architecture combined with wing-mounted conventional and distributed propulsion system integration. The primary energy carrier is SAF and the secondary energy carrier is batteries. The supplied power ratio is 0.1 and the shaft power ratio is 0.9.
Configuration 3	A high wing aircraft, with a T-tail, and a parallel propulsion system combined with a conventional propulsion system integration. The primary energy carrier is SAF and the secondary energy carrier is batteries. The supplied power ratio is 0.2 and the shaft power ratio is 0.0.

In order to quantitatively assess the weight associated with each aircraft concept, a class I weight estimation was used to find the approximate maximum take off mass. Sustainability was based upon how much fuel each configuration required for the entire mission, which was also be estimated using the class I weight estimation and a simplified energy mission analysis. The mission analysis used energy fractions for every mission segment, finds the total energy required and thereafter the fuel and battery weight. This method was found to be sufficient for small supplied power ratio inputs. Technology readiness and operations were based upon literature studies. Lastly, the cost was estimated by analysing the production costs and comparing the concepts to each other to find the relative difference in cost using the manufacturing cost breakdown presented by Willcox in reference [48].

The initial maximum takeoff mass, fuel weight and production cost estimations for the three aircraft configurations being analysed are presented in Table 2.6. As shown in this table, Configuration 1 has by far the highest maximum takeoff mass and fuel weight, while Configurations 2 and 3 are similar.

For costs, Configuration 3 was chosen as the baseline concept and the other two configurations were compared against this concept. The production costs were analysed based on the labour and material required for producing a part such as the wing or empennage. Configuration 2 has a slightly smaller wing surface area than Configuration 3, while also having a conventional tail instead of a T-tail. The wing and empennage combined amount for almost 40% of the production costs [48]. Hence, these are the main reasons why the productions costs are lower for Configuration 2.

Table 2.6: Maximum takeoff mass, fuel weight and production cost estimations for the three aircraft configurations

	Maximum takeoff mass [kg]	Fuel weight [kg]	Production cost
Configuration 1	30700	3373	+ 0.1%
Configuration 2	27069	2945	-1.3%
Configuration 3	27022	3105	Baseline concept

The secondary trade-off scores are presented in Table 2.7. Configurations 2 and 3 were given the same score for weight and sustainability because the maximum takeoff mass and fuel weight were similar. The TRL was estimated through a review of available literature. First, the series powertrain architecture with a hybrid electric propulsion system is generally assigned a TRL of 5-7 [29]. Secondly, the parallel powertrain architecture with a hybrid electric propulsion system is typically given a TRL of 2-5 [29]. Lastly, while the series/parallel hybrid architecture offers the advantage of being more generalized, it also increases the complexity. The TRL of the series/parallel architecture was therefore assumed to be limited by that of the parallel architecture, with a TRL of around 2-3. Consequently, configuration 1 has the highest score for TRL and the remaining configurations have low scores. Cost scores were accordingly assigned to each configuration using the production cost analysis.

Table 2.7: Secondary trade-off scores for the three aircraft configurations

Configuration	Weight	Sustainability	Technology Readiness	Cost	Operations	Total
Configuration 1	2	3	5	3	5	66
Configuration 2	5	5	1	5	4	76
Configuration 3	5	5	1	4	4	74

Concerning operations, it is somewhat difficult to make predictions at this current stage, as the primary differences between the three configurations under consideration are their propulsion system architectures and their wing and tail configurations. The systems involving a parallel architecture were assigned lower scores for operations due to the higher number of components that are anticipated for these systems (resulting from the mechanical coupling). This is expected to yield a higher maintenance requirement. Because it is unclear at this time whether any significant operations-related advantages may be exploited from the series/parallel architecture as a result of the application of smart power-delivery schedules, this benefit has been neglected and it has been assigned the same score as the parallel architecture. The scores for operations have also been kept relatively similar between the three configurations as it was considered difficult to apply a quantitative assessment of each configuration's effects on operations. A low weighting was also used for this category as a result of this.

As can be seen from Table 2.7, configuration 2 has the highest total score, though configuration 3 has a very close score. The only reason why configuration 2 won is because of its lower production costs, thanks to its conventional tail and smaller wing surface area. The hybrid electric aircraft is already expected to cost more than a conventional aircraft, hence the configuration with the lowest price is desired such that airlines will purchase the aircraft. In the subsystem level trade-off, the series/parallel propulsion system architecture also won the trade-off due to its increased safety and lower weight.

3
Technical Implementation

3.1. Design and Analysis Procedure

Figure 3.1 provides an outline of the procedure that was taken during the design of the aircraft of this project. After completing the trade-offs, a constraint analysis was performed to obtain the wing and power loading requirements design was iteratively developed through a loop that started with a weight estimation for the aircraft. At the beginning of the iterations, an initial value for the maximum takeoff mass was provided and convergence was determined by ensuring that the normalized difference between the maximum takeoff mass of the two most recent iterations is sufficiently small. The inputs to this design tool correspond to the top-level requirements and key parameters of each discipline.

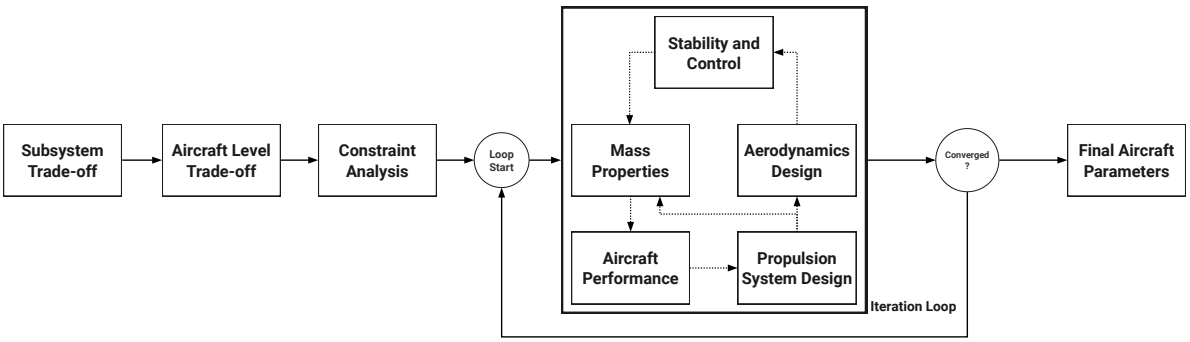

Figure 3.1: Design process flow chart.

After converging on a design, the final aircraft parameters were used to develop technical drawings, which are contained in Appendix A. The most important aspects of this design that remain to be accounted for are the preliminary design of the high-lift devices, control surfaces, wing-box structure, propellers, and battery thermal management system. Moreover, the design activities that were completed for this project are largely still at a conceptual level and thus low-fidelity methods were applied for all systems. Thus, the detailed design of all components remains to be completed and it is anticipated that the results of this analysis are suitable for a preliminary approximation only.

3.2. Constraint Analysis

The aircraft to be designed for FutPrInt50 is subject to several performance requirements. These are listed in Table 3.1. In order to size the aircraft wings and power plant, these requirements are rewritten in terms of wing and power loading. This allows the design space to be plotted, and the most optimal design point to be quantified. Most of these requirements can readily be applied in constraint analysis, while other first have to be transformed in another form.

Table 3.1: Relevant requirements for the constraint analysis.

Designation	Requirement
FP-04	The cruise speed shall be lower than Mach 0.48.
FP-06	The rate of climb shall be at least 1850 ft/min (9.4 m/s).
FP-08	The maximum operating altitude shall be 7620 m.
FP-09	The aircraft shall be able to operate on runways with a length of 1000 m or less.

FP-04 will be used as a constraint for the maximum speed the aircraft can achieve in level flight. Since the requirement stipulates a maximum cruise speed, this will be taken as the maximum speed. This will be combined with the requirement for maximum operating altitude (**FP-08**), such that the aircraft can reach its maximum speed at any altitude. As the speed of sound at 7620 m is 309.7 m/s, the maximum speed equals 148.6 m/s. Although technically possible, the requirements for stall speed (**PRF-01** and **PRF-02**) will not be added to the wing and power loading graphs. This is because the main reason for setting a stall speed is to be able to land and take-off with a reasonable speed and within a certain distance. However, these are already separate requirements, namely **FP-09**. After taking these considerations into account, the constraints in Table 3.2 were obtained.

Table 3.2: Constraints used to size the aircraft.

Constraint	Value
Take-off distance	1000 m
Landing distance	1000 m
Rate-of-climb	9.4 m/s
Maximum speed	148.6 m/s

Constraint analysis was done using the method proposed by de Vries et. al. [45], who modified the classical constraint analysis to be applicable to hybrid aircraft design, possibly including distributed propulsion. This method takes into account the aero-propulsive interactions between wing and distributed propulsion, allowing higher wing loadings. Both the distributed propulsion and primary propulsion units are sized separately. Figure 3.2 shows the wing and power loading diagrams for the conventional and distributed propulsion systems. In both cases, the wing loading (3970 N/m^2) is driven by the landing distance, and is much higher than reference aircraft due to the lift augmentation of the distributed propulsion. The power loading is constrained by different requirements for the conventional (0.0687N/W) and distributed propulsion (0.0848 N/W) systems. This is because different shaft power ratios are used at different flight phases, see Table 3.8. In cruise, all the shaft power is provided by the conventional propulsion system, which is also the sizing criterion. During take-off, a large part of the power comes from the DP system, which is driving its size.

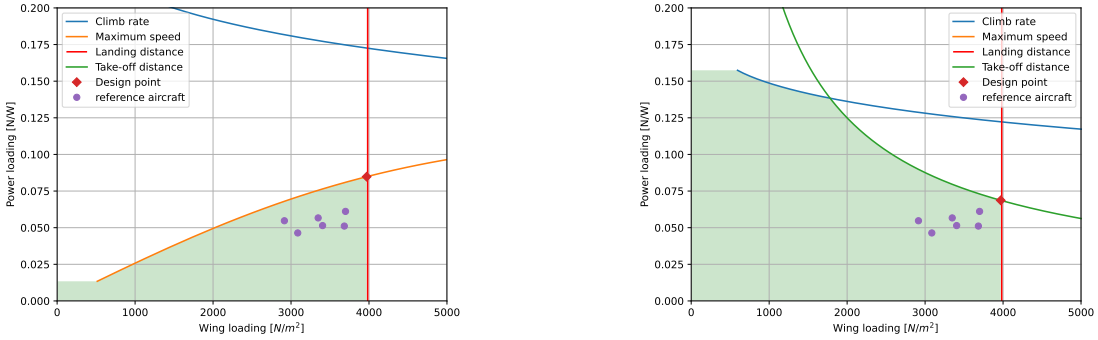

(a) Conventional propulsion system

(b) Distributed propulsion system

Figure 3.2: Wing and power loading diagrams for both propulsion systems

3.3. Aerodynamic Design

3.3.1. Airfoil Selection

The airfoil thickness ratio is estimated in the preliminary sizing phase. As suggested by Torenbeek, the thickness ratio of subsonic aircraft wings is typically between 0.15 and 0.2 [40]. Thus, a thickness ratio of 0.18 was chosen for the investigation. Five airfoils were chosen for the analysis, which are shown in the top row of Table 3.3. They were analysed using XFOIL at the cruise Mach number of 0.48, with a fixed transition point at 5% chord (assuming mainly turbulent flow due to the propeller-wing interaction). The mean aerodynamic chord was used to find Reynolds number of 1.5884×10^7. The

design C_l is determined as suggested by López et. al. [21]. Equation 3.1 shows the conversion of 3D wing lift coefficient to 2D airfoil lift coefficient. The design lift coefficient is approximately 0.46.

$$C_{l_{\text{des}}} = \frac{C_{L_{\text{des}}}}{\cos^2 \Lambda_{LE}} \tag{3.1}$$

Table 3.3: Characteristics of the five airfoils under consideration.

	E549	E1211	NACA 23018	NACA 63(3)-618	NASA SC(2)-0518
L/D_{des}	1.00	0.98	0.96	0.99	0.93
$C_{m_{des}}$	0.63	0.89	0.03	1.00	0.91
$C_{l_{Max}}$	0.77	0.91	0.93	0.91	1.00
$C_{d_{min}}$	1.00	0.98	0.98	0.99	0.92
$(C_l - C_{l_{\text{des}}})$ at $C_{d_{\text{min}}}$	0.38	0.37	0.29	0.45	1.00
Drag slope	0.33	0.30	0.25	0.33	1.00
Total	18.2	19.1	16.0	20.2	25.0

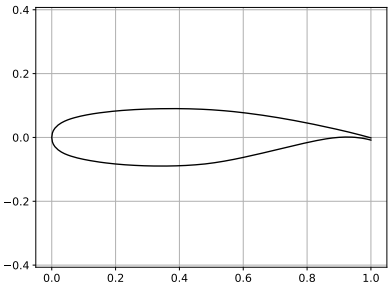

Figure 3.3: NASA SC(2)-0518 airfoil profile

The selection criteria also corresponds to information from López et. al. in [21]. The drag slope is the change of drag coefficient around the design C_l. This way, the design C_l can be ensured within or near the drag bucket range. On the other hand, the values in the Table 3.3 are normalised. Values to maximise were normalised by the highest value in the row and values to minimise were first inverted and then normalised by the largest result. The airfoil variation along the wing has also not been considered at this stage. As a result, the NASA SC(2)-0518 supercritical airfoil was found to be suitable.

3.3.2. Main Wing Planform Design

The wing platform design is based on the methods suggested by classical aircraft design books, including Raymer [28], Torenbeek [41, 40], and Roskam [30]. The surface area, aspect ratio, taper ratio, twist angle, and dihedral angle were determined. First, the maximum takeoff weight and the wing loading were used to find the wing surface area. Secondly, the aspect ratio was chosen to be 12 based on ATR-72, as the design is also a regional turboprop aircraft with similar characteristics. Thirdly, the taper ratio was determined based on empirical data as shown in the Figure 3.4.

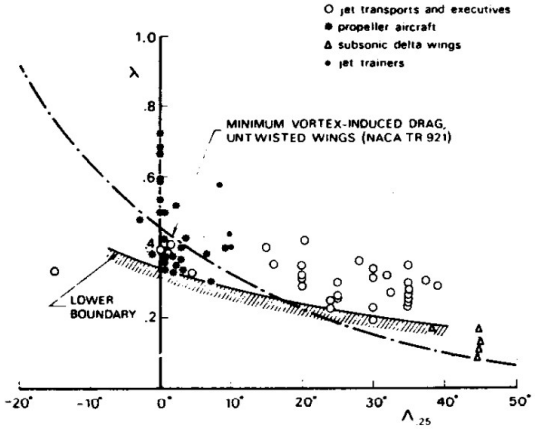

Figure 3.4: Taper ratios for wings with differing quarter-chord sweep angles according to Torenbeek [41].

Table 3.4: Main wing planform parameters

Aspect ratio	12.00	[-]
Taper ratio	0.450	[-]
$0.25c$ sweep angle	0.000	[deg]
Wing area	61.57	[m^2]
Root chord	3.124	[m]
Tip chord	1.406	[m]
MAC length	2.373	[m]
MAC spanwise location	5.936	[m]
Wing span	27.18	[m]
Dihedral angle	5.000	[deg]
Tip incidence angle	-3.000	[deg]

Zero quarter-chord sweep was applied in order to reduce the weight and the length of the nacelles for the distributed propulsion system; moreover, the cruise speed is in the low-subsonic regime. As a result of the zero-valued quarter-chord sweep, the taper ratio was set to 0.45. In addition, a twist angle of the $-3°$ was defined, as it was suggested within [28] to provide adequate stall characteristics. Furthermore, the combination of the selected taper ratio and the empirical twist angle is expected to yield a lift distribution as close as possible to the elliptical distribution. On the other hand, the dihedral angle was chosen to

achieve stability in sideslip conditions. Equation 3.2 shows the relationship between dihedral angle and sweep angle for a low wing according to [28], and thus a dihedral angle of 5° was determined.

$$\Gamma = 3 - \frac{\Lambda_{c/4}}{10} + 2 \tag{3.2}$$

The remaining wing planform parameters have been computed with the aforementioned ratios and angles and are shown in Table 3.4. The simplified trapezoidal wing geometry relations from the design books in [28, 30, 40, 41] were used for calculating the root chord, tip chord, and wing span. The pitching moment of mean aerodynamic chord (MAC) is essentially constant for any angle of attack, and may be readily computed using established parameters. The mean geometric chord (MGC) was also assumed to be equivalent to the MAC in this case, and the spanwise location was found as well. On the other hand, the wing spars were chosen to be placed at 20% and 75% chord from the leading edge, as suggested by Raymer in [28], and to ensure that sufficient space is available for the fuel tanks.

3.3.3. Aerodynamic Performance

Class II drag estimation

A class II drag estimation was performed on the aircraft. The method proposed by Roskam in [30] was used. Here, the lift-dependent and lift-independent drag values are calculated separately. The zero-lift drag consists of skin friction calculations and estimations of interference drag. For the skin friction drag, the component was approximated by a flat plate with an equivalent Reynolds number and wetted area. Interference drag came from semi-empirical relations. Lift-dependent drag was assumed to be proportional to the square of the lift coefficient. The lift-to-drag ratio for a range of lift coefficients is plotted in Figure 3.5a. It is indicated that the aircraft does not cruise at its optimum L/D. The plot has been produced for the maximum cruise Mach number of 0.48 from the requirements, it would however be more fuel efficient to cruise somewhat slower (around Mach 0.38). Nonetheless, this would reduce the productivity of the aircraft as less trips would be made per day. The required power both for the aircraft with and without the effects of propeller integration is shown in Figure 3.5b. Note that the difference between the two is non-existent. This is because during cruise, the shaft power ratio is virtually zero, resulting in all the power being provided by the gas turbines, for which the interaction has not yet been implemented at this stage. Figure 3.5c shows the drag breakdown of the aircraft at a cruise Mach of 0.48 and an altitude of 5200 meters. Unsurprisingly, the wing is responsible for the largest drag of the aircraft. In a later design stage, it would be useful to perform a multidisciplinary optimisation of the wing planform to decrease the drag while maintaining the geometric and lift-performance requirements, as this would have an important influence on the overall performance of the aircraft. The drag estimation was validated by comparing results obtained with a configuration resembling the ATR-72 to the results from [23]. This procedure has been considered sufficient for this project, as the anticipated in-flight conditions of the ATR-72 are comparable to the requirements for this project.

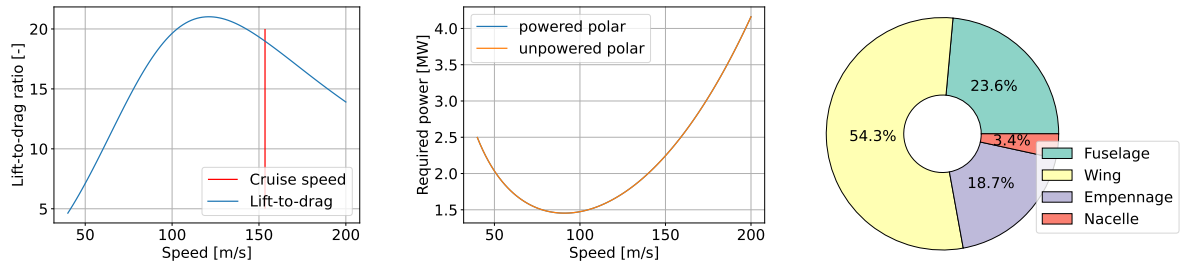

(a) Lift-to-drag ratio vs speed in cruise. **(b)** Required power vs speed in cruise. **(c)** Drag contributions in cruise.

Figure 3.5: Aerodynamic performance of the aircraft in cruise.

3.4. Stability and Control

3.4.1. Tail Sizing

The tail was sized using Roskam's preliminary sizing method, using the tail volume, where the tail volume is based on statistics. The tail volume was picked based on the class I maximum takeoff mass

and wing area. With the tail volumes defined, the surface area of the horizontal tail and vertical tail can be found using Equation 3.3 and Equation 3.4, respectively [31]. The aft centre of gravity, X_{afcg}, is found using the methodology presented in Section 3.4.2. The distance between the nose of the aircraft and the respective tail centre of gravity location, X_h and X_v, is calculated using an iterative procedure. The goal of the iterative procedure is to place both the vertical and horizontal tail as close to the end of the tail of the aircraft as possible. This is to ensure a larger tail arm to help with balancing the aircraft due to the large additional battery weight in front of the aft centre of gravity. The rest of the tail can be sized using the same equations applied during the wing sizing.

$$\bar{V}_h = \frac{(X_h - X_{afcg})\, S_h}{Sc} \tag{3.3}$$

$$\bar{V}_v = \frac{(X_v - X_{afcg})\, S_v}{Sb} \tag{3.4}$$

The final horizontal and vertical tail parameters can be found in Table 3.5. The aspect ratio, taper ratio, and sweep angles are based on literature. The aspect ratio of the horizontal tail is typically between 3 and 5, and the aspect ratio for the vertical tail usually lies between 1 and 2. While a higher aspect ratio can help in reducing the stall angle of attack of the aircraft and increases the effectiveness, it also increases tailplane weight. Thus, it was opted to pick an aspect ratio of 4 for the horizontal tailplane to have a balance between the effects of the aspect ratio. For the vertical tail, an aspect ratio of 2 was chosen. This was to allow for a higher vertical tail effectiveness. A large difference in weight was also not observed between an aspect ratio of 1 and 2. The taper ratio of the horizontal tail is usually between 0.3 and 1, whereas the taper ratio for the vertical tail is in the range of 0.3 to 0.7. While a smaller taper ratio does decrease the weight of the tailplane and could reduce tip stall, it was chosen to opt for a higher taper ratio for both the vertical and horizontal tail. This was to ensure that the vertical and horizontal tail did not have a root chord larger than the tail cone because otherwise it would interfere with the cabin. Lastly, turboprops are always sized with a 0° $3/4c$ sweep angle for the horizontal tail. The vertical tail for a turboprop typically has a leading edge sweep angle between 0° and 50°. A larger sweep angle increases the moment arm, while also decreasing the effectiveness of the tailplane. The larger moment arm is desired for this aircraft, however, the effectiveness of the tail should also not be compromised too much. Thus a leading edge sweep angle of 30° was chosen.

Table 3.5: Horizontal and vertical tail parameters

Horizontal tail		Vertical tail	
Tail volume [-]	1.075	Tail volume [-]	0.083
Aspect ratio [-]	4.00	Aspect ratio [-]	2.00
Taper ratio [-]	0.60	Taper ratio [-]	0.70
$3/4c$ sweep angle [°]	0.00	Leading edge sweep angle [°]	30.0
Tail area [m^2]	18.9	Tail area [m^2]	12.3
Root chord [m]	2.72	Root chord [m]	2.92
Tip chord [m]	1.63	Tip chord [m]	2.04
Span [m]	8.71	Span [m]	4.96

3.4.2. Centre of Gravity

The centre of gravity of the aircraft is calculated using Roskam's class I centre of gravity method [31]. Here, centre of gravity fractions are assumed for different components of the aircraft, such as the wing, fuselage, and empennage. Using these fractions, along with the weight of the components, the fuselage group centre of gravity with respect to the nose of the aircraft can be found. The wing group centre of gravity, as a function of the wing mean aerodynamic chord, can also be estimated.

Thereafter, it is possible to estimate the position of the leading edge of the wing mean aerodynamic chord with respect to the nose of the aircraft using Equation 3.5. X_{FCG} is the fuselage group centre of gravity, $\left(\frac{x}{\bar{c}}\right)_{\text{WCG}}$ is the wing group centre of gravity, M_{W} is the mass of the total wing group and M_{F} is the total mass of the fuselage group. Moreover, $\left(\frac{x}{\bar{c}}\right)_{\text{OEWCG}}$ is the operational empty weight centre of gravity with respect to the wing mean aerodynamic chord, which can be assumed to be $0.25\bar{c}$ [31].

$$X_{\text{LEMAC}} = X_{\text{FCG}} + \bar{c}\left[\left(\frac{x}{\bar{c}}\right)_{\text{WCG}} \frac{M_{\text{W}}}{M_{\text{F}}} - \left(\frac{x}{\bar{c}}\right)_{\text{OEWCG}} \left(1 + \frac{M_{\text{W}}}{M_{\text{F}}}\right)\right] \tag{3.5}$$

Having found the X_{LEMAC}, the most forward and aft centre of gravity were found by determining the centre of gravity of the following weight combinations: W_{OE}, $W_{\text{OE}} + W_{\text{payload}}$, $W_{\text{OE}} + W_{\text{payload}} + W_{\text{fuel}} + W_{\text{battery}}$, and $W_{\text{OE}} + W_{\text{fuel}} + W_{\text{battery}}$. The fuel is located in the wing and the battery is assumed to be located in front of the wing box, in the middle of the fuselage. The forward and aft centre of gravity may be identified from Figure 3.6. As shown, the forward centre gravity occurs at a weight of W_{OE}, where $x_{\text{fwd,cg}} = 8.96$ m, and the aft centre occurs for $W_{\text{OE}} + W_{\text{fuel}} + W_{\text{battery}} + W_{\text{payload}}$, with $x_{\text{aft,cg}} = 9.46$ m.

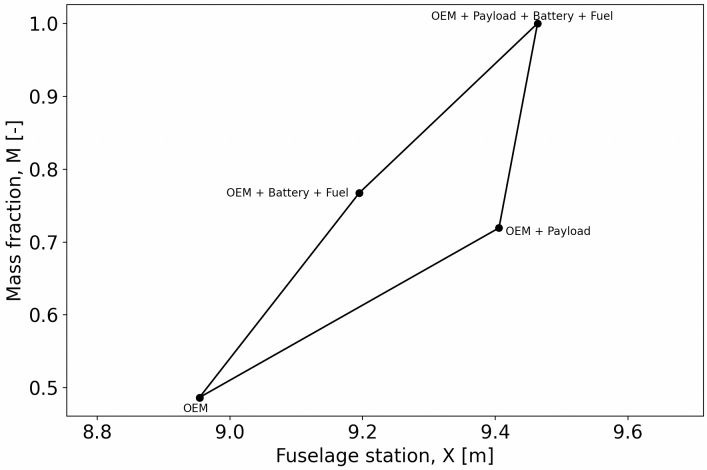

Figure 3.6: Centre of gravity for the following four weight combinations: W_{OE}, $W_{\text{OE}} + W_{\text{payload}}$, $W_{\text{OE}} + W_{\text{payload}} + W_{\text{fuel}} + W_{\text{battery}}$, and $W_{\text{OE}} + W_{\text{fuel}} + W_{\text{battery}}$

3.4.3. Landing Gear

The landing gear is sized to ensure the aircraft does not tip over, both longitudinally and laterally. To ensure longitudinal stability on ground, the scrape angle has to be less than or equal to the tip over angle. Both were chosen to be 15°. For lateral stability, the overturn angle has to be less than or equal to 55°, which is met by ensuring a sufficiently wide main landing gear track. Moreover, a minimum propeller clearance of 5° and a minimum tip clearance of 5° is also used to position the main landing gear [43]. It is assumed that the nose landing gear carries 12% of the maximum takeoff weight. This is to ensure adequate steering capabilities [43]. The main landing gear therefore carries 88% of the maximum takeoff weight. These percentages are used to find the required wheel dimensions and nose wheel location. The maximum takeoff weight must be balanced by the landing gear, and with the main landing gear already placed, the nose landing gear was positioned accordingly. The final landing gear parameters are shown below in Table 3.6.

Table 3.6: Landing gear dimensions

	Main landing gear	**Nose landing gear**	**Overall landing gear**	
Wheel dimensions (British size) [m] (outer diameter x width - inner diameter)	0.84 x 0.25 - 0.41	0.44 x 0.14 - 0.19	Track width [m]	3.6
Number wheels [-]	4	2	Min required track width [m]	2.9
Static load per wheel [kg]	5484	1496	Clearance angle [°]	15
Location (from nose) [m]	10.5	2.1	Absorber stroke length [m]	0.2
Strut length [m]	1.3	1.5		

3.4.4. Static Margin

The static margin was determined by assessing the stick fixed stability of the aircraft as a function of x_{cg}/MAC and the horizontal tail surface area to the wing surface area fraction, S_h/S. The minimum static margin was chosen to be 5% MAC. This is typically a good value as it can indirectly account for stick-free and minimum control force limits [24]. With this static margin, the stability criteria is also met for the forward and aft cg. The aft cg puts a limit on the maximum static margin. It was determined that the maximum attainable static margin is 19% MAC.

3.5. Propulsion System Design

3.5.1. Powertrain Modelling

To model the powertrain system, the following schematic diagrams were used to represent the primary and secondary groups of components within the distributed propulsion system, as suggested by de Vries et. al. in [45]. The equations used to represent the hybrid-electric propulsion system were generalized to be applicable to the series-parallel partial hybrid configuration. Figure 3.7 contains a simplified schematic diagram of the propulsion system architecture that was considered during this project. It is possible to model any type of hybrid-electric engine architecture using this model [45].

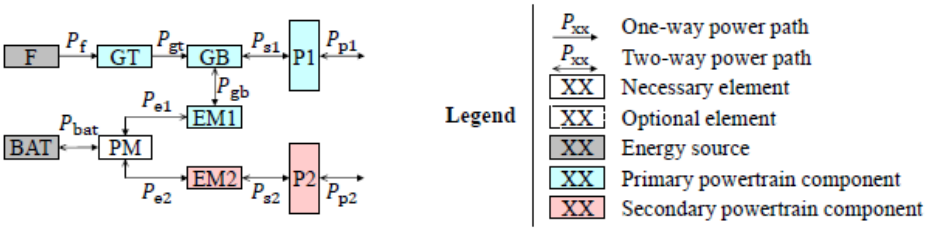

Figure 3.7: A schematic diagram of the propulsion system architecture considered during this project (adapted from [45]).

Corresponding to each component in the series-parallel partial hybrid diagram, the efficiencies for each component are shown in Table 3.7. In addition, the propulsive efficiency values were approximated in each mission segment using actuator disk theory also accounting for profile losses. The values used are motivated by general trends observed in [6, 16, 45]. Equation 3.6 was then used to obtain the power at each component of the propulsion system based on the wing- and power-loading requirements.

Table 3.7: A summary of the efficiency values used during this project for the hybrid-electric powertrain.

Powertrain Component	Abbreviation	Efficiency Value [%]
Gas Turbine	GT	30
Gearbox	GB	96
Power Distribution Module	PM	99
Primary Electric Motor	EM1	96
Secondary Electric Motor	EM2	96
Primary Propulsive	P1	75 – 90
Secondary Propulsive	P2	70 – 85

Note that the abbreviations “S1” and “S2” respectively refer to the primary shaft and the secondary shaft. The power values obtained are used during the component sizing and mission analysis.

$$\begin{pmatrix} 0 \\ 0 \\ 0 \\ 0 \\ 0 \\ 0 \\ 0 \\ 0 \\ 0 \\ P_p \end{pmatrix} = \begin{pmatrix} -\eta_{GT} & 1 & 0 & 0 & 0 & 0 & 0 & 0 & 0 & 0 \\ 0 & -\eta_{GB} & 1 & 1 & 0 & 0 & 0 & 0 & 0 & 0 \\ 0 & 0 & 0 & -\eta_{P1} & 0 & 0 & 0 & 0 & 1 & 0 \\ 0 & 0 & -\eta_{EM1} & 0 & 1 & 0 & 0 & 0 & 0 & 0 \\ 0 & 0 & 0 & 0 & -\eta_{PM} & -\eta_{PM} & 1 & 0 & 0 & 0 \\ 0 & 0 & 0 & 0 & 0 & 0 & -\eta_{EM2} & 1 & 0 & 0 \\ 0 & 0 & 0 & 0 & 0 & 0 & 0 & -\eta_{P2} & 0 & 1 \\ 0 & \Phi & 0 & 0 & 0 & (\Phi - 1) & 0 & 0 & 0 & 0 \\ 0 & 0 & 0 & \varphi & 0 & 0 & 0 & (\varphi - 1) & 0 & 0 \\ 0 & 0 & 0 & 0 & 0 & 0 & 0 & 0 & 1 & 1 \end{pmatrix} \begin{pmatrix} P_F \\ P_{GT} \\ P_{GB} \\ P_{S1} \\ P_{EM1} \\ P_{BAT} \\ P_{EM2} \\ P_{S2} \\ P_{P1} \\ P_{P2} \end{pmatrix} \tag{3.6}$$

3.5.2. Hybrid-Electric System Architecture

An important aspect of the hybrid-electric system architecture is defining the supplied power ratio and shaft power ratio. The shaft power ratio and supplied power ratio are defined by Equation 3.7 and Equation 3.8, respectively. Both of these ratios have a large impact on the fuel weight and battery weight, as well as the maximum take-off weight. During the most energy intensive phase (climb and cruise), a large supplied power ratio can adversely affect the fuel weight as batteries add a considerable amount of weight to the design, even when taking future technology levels into consideration. As such,

it is nearly impossible to achieve a fuel weight for the whole aircraft mission that is lower than existing regional turboprops. Thus, instead of attempting to minimise the total fuel weight across the whole mission, it was decided to minimise the fuel weight for the mission segments occurring closest to the airport, such as takeoff and climb. This will reduce overall greenhouse gas emissions close to the airport. Most importantly is the reduction of nitrogen oxides, which are primarily emitted at high turbine inlet temperatures (typically during takeoff and climb for a conventional aircraft configuration) [10].

$$\varphi = \frac{P_{s2}}{P_{s2} + P_{s1}} \tag{3.7}$$

$$\Phi = \frac{P_{bat}}{P_{bat} + P_f} \tag{3.8}$$

Five different hybrid-electric powertrain configurations were investigated. Each configuration has a different number of distributed propulsors, in addition to unique supplied power ratio and shaft power ratio values. These are summarised in Table 3.8. The values are the same for the diversion segments. For these configurations, the fuel weight during mission segments close to ground were compared.

Table 3.8: Hybrid-electric system architecture configurations

		Configuration 1	Configuration 2	Configuration 3	Configuration 4	Configuration 5
Number of distributed propulsors		8	8	6	10	10
Supplied power ratio	Taxi	1.00	1.00	1.00	1.00	1.00
	Takeoff	0.05	0.10	0.05	0.15	0.30
	Climb	0.05	0.10	0.05	0.15	0.30
	Cruise	0.00	0.00	0.00	0.00	0.00
	Descent	0.05	0.10	0.05	0.10	0.30
	Loiter	0.00	0.00	0.00	0.00	0.00
Shaft power ratio	Taxi	0.00	0.00	0.00	0.00	0.00
	Takeoff	0.50	0.70	0.50	0.70	0.80
	Climb	0.90	0.70	0.90	0.90	0.60
	Cruise	0.00	0.00	0.00	0.00	0.00
	Descent	0.05	0.90	0.05	0.90	0.60
	Loiter	0.00	0.00	0.00	0.00	0.00

The mission segments close to ground were chosen to be taxi out, takeoff, climb, descent and taxi in. While climb and descent are at one point far from the ground, they do both also occur close to ground, whether that is at the beginning of climb or at the end of the descent. Moreover, as already mentioned, climb typically also emits a large quantity of nitrogen oxides compared to, for example, cruise. Therefore, both of the segments were also analysed for minimising fuel weight.

Table 3.9: Fuel weight for mission segments close to ground for the different hybrid-electric system architecture configurations

Fuel weight [kg]	Configuration 1	Configuration 2	Configuration 3	Configuration 4	Configuration 5
Taxi out	0.00	0.00	0.00	0.00	0.00
Takeoff	3.85	3.54	3.87	3.57	1.77
Climb	253	184	252	203	98.8
Descent	0.00	0.00	0.00	0.00	0.00
Taxi in	0.00	0.00	0.00	0.00	0.00
Total	257	188	256	207	101

The fuel weights for the mission segments close to ground for all five hybrid-electric system architecture configurations are shown in Table 3.9. Note that these values are based upon the class I weight estimation and are therefore not final. As can be seen, configuration 5 has the lowest total fuel weight close to ground. Thus, configuration 5 was chosen for the hybrid-electric system architecture.

3.5.3. Battery Sizing

Having determined the hybrid-electric system architecture configuration and having found the total energy and power required for the complete mission, using the methodology presented in Section 3.7.2, makes it possible to size the battery. First of all, it is desired to have a battery with a long life, such that it does not have to be replaced as often. In order to do so, it is recommended to never complete full cycles, i.e. only partially charge and discharge the batteries [37]. A minimum state-of-charge of 20% is recommended [44]. Moreover, a maximum SOC of 90% has been chosen since completely discharging the battery can have a negative effect on the capacity after a number of cycles [8]. Lithium-ion batteries also have a storage efficiency of 85% [20]. Taking into account the SOC and storage

efficiency, it means that the energy at the end of the life of the battery has to be larger than the actual energy required from the battery. The battery power is found using Equation 3.6. The mission segment with the highest battery power is used to size the battery for the power requirement, such that the power requirement is always met. Dividing the battery power by the battery specific power at pack level found in Table 3.12 yields the battery weight for the power requirement.

For the design range, the battery power requirement is the most constraining. Hence, the battery weight comes from the battery power. The battery needs to provide 11446.5 kWh, which is used to design the battery pack, starting at a cell level. The battery is sized by choosing a voltage to achieve at cell level and thereafter estimating the necessary capacity using the voltage. Typical lithium-ion batteries have 3.7 V per cell, though this can be increased by placing the cells in series [13]. It was chosen to place 20 layers of cells connected in parallel. Within each layer, there are 216 cells connected in series. This will generate approximately 800 V, meaning that 14308 Ah is required. The 800 V seems to be feasible to a battery designed to be used on aircraft, when looking at Airbus' battery for EcoPulse [5]. Assuming a cell is able to provide 2.6 Ah [13], the 20 layers of cells connected in parallel will provide a total of 52 Ah. This is one module. To achieve the ampere-hours required, 106 modules will be connected in parallel. By using several modules, it also makes it easier to replace part of the battery in case a cell fails. Only the module with the failed cell would have to be replaced in the pack.

The C-rate specifies the current at which the battery is being charged or discharged at. It can be found by specifying the time to charge or discharge [36]. A longer time to charge or discharge means a lower C-rate. It has therefore been concluded that the maximum C-rate will be defined by how quickly the battery should be charged during turnaround. Turnaround times for short-haul flights are approximately 30 minutes [14]. To meet this standard, a maximum C-rate of 2C is necessary.

The final battery specifications are listed in Table 3.10.

Table 3.10: Battery specifications for design range and DOC mission

	Design Range	DOC Mission
Battery energy required [MJ]	2636	2553
Battery end-of-life energy [MJ]	4431	4292
Battery power required [kW]	4680	4538
SOC	20% - 90%	
Battery efficiency	85%	

Voltage of cell [V]	3.7
Capacity of cell [Ah]	2.6
Number of cells per layer [-]	216
Number of layers [-]	20
Number of modules [-]	106
Maximum C-rate [-]	2C

3.5.4. Engine Selection

Electric Motors

The electric motors are found based on the maximum power required per motor over the entire mission. A database of different electric motors for aviation was made. The motor whose power was closest, but still higher than the required power was selected. Since the masses of the different motors found differed significantly, and because it was unclear which components of the powertrain were included in the mass, this was not a consideration for the selection of the motor. A required power per engine of 356 kW was found. Using the method above, this lead to the Helix SPM242-176 as the most suitable motor. Some basic parameters about it are given in Table 3.11.

Table 3.11: Some parameters about the SPM242-176, taken from the manufacturers website [38].

Maximum power [kW]	450
Continuous power [kW]	228
Weight [kg]	47.9

Gas Turbine

The gas turbine was found according to the maximum required power to be provided by the gas turbine. Concerning the propulsion system architecture provided in Figure 3.7, the minimum allowable rated power of the conventional engine was taken as $P_{\text{GT}} \times \eta_{\text{GB}} / N_{\text{engines}}$. A value of 1637 *kW* or 2195 shp was obtained for each turboprop engine. The minimum rated power for each engine was then rounded up to 1640 kW or 2200 shp. With relatively few engines that satisfy the power requirement outside of the

PW100/150 series and even less that are at least 50% SAF compatible, it was found to be important that the chosen engine has been demonstrated to be at least partially SAF compatible. It was considered necessary for the rated power of the chosen engine to be considerably above the required power to ensure that there is always enough power available to satisfy requirements at each mission segment.

The engine that was selected is the PW127XT from Pratt and Whitney Canada. This engine has an approximate uninstalled mass of 420 kg, and it currently is the first turboprop to have been proven to be capable of flying on 100% SAF after a recent flight test with the ATR-72, which has very similar characteristics to the aircraft of this project [27]. Pratt and Whitney has plans to continue to develop this engine to be 100% compatible with SAF, and thus it is likely that it will be suitable for this aircraft by its entry-into-service date [27]. The PW127XT engine was found to have an approximate installed mass of 635 kg according to the method of [19]. This was considered reasonably close to the target mass of 575 kg that was obtained using the statistical techniques that were applied in Equation 3.12 and Equation 3.13. Moreover, it may be possible to yield a lower installed engine mass using next-generation materials or techniques, although this has not been factored into the decision-making process. This engine also satisfies the aircraft's power requirement of 2200 shp by a margin of 25%, as it has a rated power of 2750 shp. This ensures that the engine will always have a sufficient amount of power to satisfy the aircraft's requirements. During later stages, more detailed design studies will need to be performed to precisely quantify the effects associated with the engine's installation. This includes higher-fidelity analyses to determine the added mass and drag penalty due to its installation onto the aircraft.

3.6. Mass Properties

3.6.1. Class I Weight Estimation

For conventional aircraft, the take-off weight of the aircraft is decomposed into the payload weight, the fuel weight, and the operational empty weight. In this case, the payload weight is a top-level requirement, and the operational empty weight is given as a fraction of the maximum take-off weight according to empirical relationships [41]. For hybrid-electric aircraft, a few unique challenges exist, which make this procedure no longer valid. First, there are no existing production-ready aircraft of this classification, which means that it is not possible to identify a trend between the maximum take-off mass and predicted operational empty mass of hybrid-electric aircraft. Second, the hybrid-electric aircraft must include a battery, and the electrical components that must be included within the powertrain cause the overall mass of the powertrain to be noticeably larger in hybrid-electric configurations [45]. Third, the wing-loading may be higher for cases involving a distributed electric propulsion system due to the dynamic pressure of the flow over the wing being higher; this could result in a lower wing weight fraction in comparison to conventional configurations [45]. Finally, due to the addition of batteries and additional electrical components, the maximum take-off weight of hybrid-electric aircraft will likely be much larger, which results in a considerable difference in wing and propulsion system weight to maintain the required wing and power loading [45]. Thus, the modified weight breakdown for the Class-I weight estimation approach that was applied for this project is shown in Equation 3.10, which is based on the typical weight breakdown that is indicated in Equation 3.9.

$$W_{\text{TO}} = W_{\text{OE}} + W_{\text{payload}} + W_{\text{fuel}} + W_{\text{batteries}} \tag{3.9}$$

$$\Rightarrow W_{\text{TO}} = W'_{\text{OE}} + W_{\text{wing}} + W_{\text{powertrain}} + W_{\text{payload}} + W_{\text{fuel}} + W_{\text{batteries}} \tag{3.10}$$

The hybrid-electric propulsion system weight was approximated with power and energy requirements for all electrical components. Power and energy density values were projected to levels that are anticipated to be possible in the year 2035. They correspond to observations made in [45, 50], and have been recorded in Table 3.12. The gearbox and power distribution module weights were neglected.

Table 3.12: Anticipated technology levels for the energy carriers that have been selected using [9, 17, 45, 50, 39, 26]

Component	Specific Energy (kJ/kg)	Specific Power (kW/kg)
Sustainable Aviation Fuel	42840	N/A
Lithium-Ion Batteries (Pack Level)	2160	1.0
Lithium-Ion Batteries (Cell Level)	1224	1.0
Electric Motor	N/A	7.7

Note, concerning the specific energy of lithium-ion batteries at pack level, 500 Wh/kg is considered conservative and 750 Wh/kg is considered optimistic for the year 2035 [17, 50]. A value of 550 Wh/kg was therefore chosen to remain reasonably conservative while considering trends in Figure 3.9a.

To obtain the traditional definition of the operational empty weight, a regression was performed with existing conventional twin engine turboprop aircraft that have a range or number of passengers that is comparable to the requirements for this project. The conventional wing and propulsion system weights were approximated using Equations 3.11 and Equation 3.13, and these weights were removed from the operational empty mass of each aircraft. A trend was used to predict the relevant weight fractions, and the wing and powertrain weights were recomputed for each configuration that was investigated during this project using the same wing and powertrain weight equations. Figures 3.8a and 3.8b contain the trends that were observed for the operational empty mass as a function of the maximum takeoff mass. These trends are consistent with trends observed in the literature, as shown in Figure 3.9b.

$$W_{\text{wing}} = 96.948 \left[\left(\frac{n_z W_{\text{TO}}}{10^5} \right)^{0.65} \left(\frac{AR}{\cos^2\left(\Lambda_{c/4}\right)} \right)^{0.57} \left(\frac{S_{\text{wing}}}{100} \right)^{0.61} \left(\frac{1+\lambda}{2\,(t/c)} \right)^{0.36} \sqrt{1 + \frac{V_H}{500}} \right]^{0.993} \tag{3.11}$$

$$W_{\text{turboprop-engine}} = \frac{P_{\text{rated}} - 110.7}{2.631} \tag{3.12}$$

$$W_{\text{powertrain}} = 2.575 W_{\text{turboprop-engine}}^{0.922} N_{\text{engines}} \tag{3.13}$$

In some cases, the uninstalled weight of the engines for each of the reference aircraft was provided by the manufacturer, and thus Equation 3.12 was not always required.

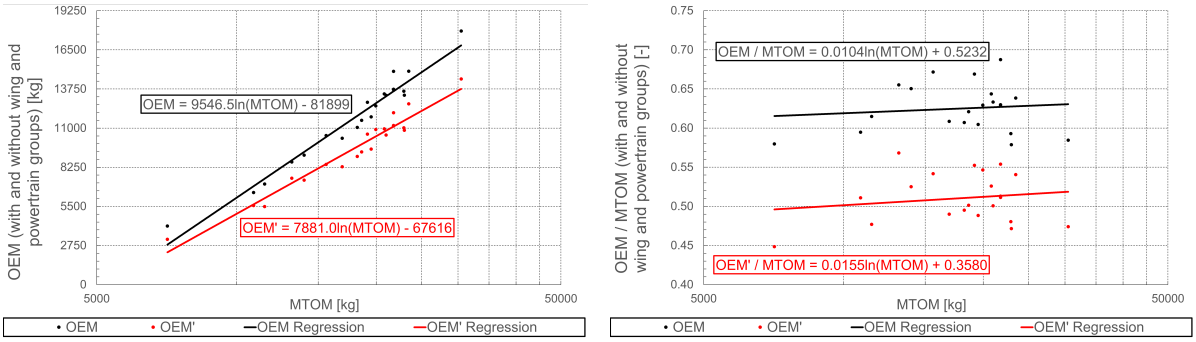

(a) Operational empty mass vs. maximum takeoff mass.

(b) Operational empty mass fraction vs. maximum takeoff mass.

Figure 3.8: Plots of regressions that were performed to obtain the operational empty mass as a function of the maximum takeoff mass for several regional aircraft with comparable range and number of passengers to the TLAR.

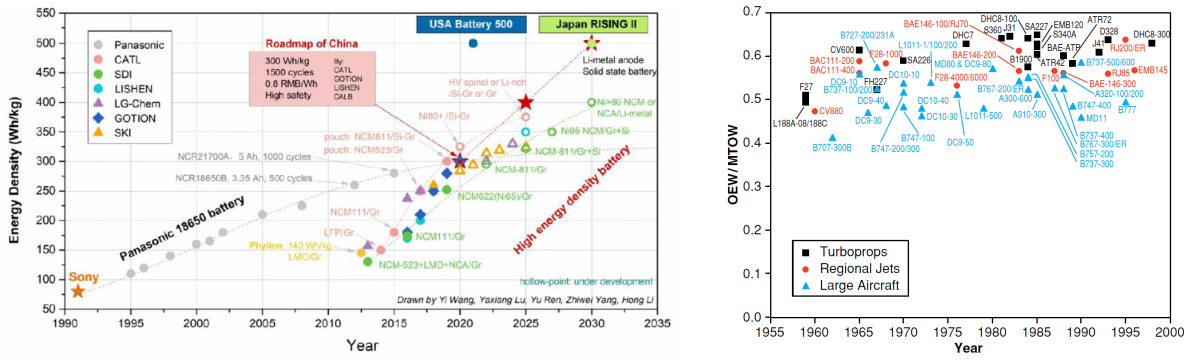

(a) Trends observed for the specific energy of batteries [7].

(b) Gross weight vs. empty weight for GA aircraft [6].

Figure 3.9: Current and projected trends that were used to support the aircraft weight estimation procedure.

All empirical relations for subsystem weights were obtained from Reference [19]. Within all these equations, imperial units must be used (i.e. lbf is required for force or weight values, ft for length values, lbf/ft^2 for pressure values, and shp for power values). Moreover, any reference airspeed is given in $KEAS$, and the ultimate load factor is defined by the *CS-25* requirement, as shown in Equation 3.14.

$$n_z = \begin{cases} 3.8 \times 1.5 & \text{if MTOW} \leq 4100 \\ \left(2.1 + \frac{24000}{\text{MTOW}+10000}\right) \times 1.5 & \text{if } 4100 < \text{MTOW} < 50000 \\ 2.5 \times 1.5 & \text{if } 50000 \leq \text{MTOW} \end{cases} \tag{3.14}$$

Finally, the operational empty mass less wing and powertrain groups was obtained using the following equation (with all units given in kg), which is also shown in Figure 3.8b. The result of this was then added to the wing and powertrain groups evaluated for each aircraft configuration under consideration to obtain the actual operational empty mass, as required for the class I weight estimation.

$$W'_{\text{OE}} = W_{\text{TO}} \left(0.0155 \ln \left(W_{\text{TO}}\right) + 0.3580\right) \tag{3.15}$$

3.6.2. Class II Weight Estimation

The equations for the class II weight estimation were taken from References [22, 28]. All equations that have been used are only valid for aircraft that fly below 300 $KTAS$, which is sufficient for this project. The operational empty weight was calculated by summing together the calculated weights of the airframe, onboard components, and powertrain groups.

The weight of the airframe was calculated by summing together masses of the wings, fuselage, vertical tail, and horizontal tail. A factor of 1.25 was also applied to the weight of the vertical tail if a T-tail was used, otherwise the equations proposed by Nicolai in Reference [22] were used, as shown below.

$$W_{\text{airframe}} = W_{\text{wing}} + W_{\text{fuselage}} + W_{\text{horizontal-tail}} + W_{\text{vertical-tail}} \tag{3.16}$$

The weight of the onboard components was accounted for through a combination of equations proposed by either Raymer or Nicolai. The equations that were selected were chosen through trial-and-error according to results obtained for aircraft with a similar number of passengers and range to that of the top-level requirements. The equations that yielded values that were closer to the actual mass fractions for aircraft with similar top-level requirements were ultimately used. The components that have been included within this calculation are indicated in Equation 3.17.

$$\begin{aligned} W_{\text{components}} = W_{\text{front-landing-gear}} + W_{\text{nose-landing-gear}} + W_{\text{hydraulic-system}} + W_{\text{fuel-system}} + \\ W_{\text{flight-control-system}} + W_{\text{avionics}} + W_{\text{electrical-system}} + W_{\text{air-conditioning}} + W_{\text{furnishings}} \end{aligned} \tag{3.17}$$

The weight of the powertrain group was obtained by summing the masses of components within the hybrid-electric propulsion system. The installed engine weight was obtained using Equation 3.13, the electric motor weight was obtained using the primary and secondary motor power values and the motor power density. The high-voltage cable weight was obtained using a cable specific power per unit length of 1.0×10^{-6} kg/W/m. Otherwise, masses of the gearbox and power distribution module were neglected. Equation 3.18 was therefore used to obtain the weight of the powertrain group.

$$W_{\text{powertrain}} = W_{\text{installed-propulsors}} + W_{\text{primary-electric-motor}} + W_{\text{secondary-electric-motor}} + W_{\text{HV-cables}} \tag{3.18}$$

In some cases, the equations provided by Raymer and Nicolai were the same and thus both were used in these cases. Reference [19] also provides a complete summary of all the weight equations used, including suggestions for how to apply these equations. It was suggested in [19] that the equations should be scaled or combined to yield appropriate values for specific applications, although the equations were not modified in this case as there are no existing hybrid-electric aircraft to compare to.

3.6.3. Battery and Fuel Weight

To calculate the battery and fuel weight of the hybrid electric propulsion system, the mission analysis was performed, as explained in Section 3.7. This provided the energy for every mission segment in the mission profile provided in Figure 3.11. The fuel weight was calculated by summing fuel weight required per mission segment, as seen in Equation 3.19. The battery weight was found using the most constraining requirement between the energy requirement and power requirement.

$$W_{\text{f,tot}} = \sum \frac{1}{e_{\text{f}}} (1 - \varphi)_{\text{i}} E_{\text{i}} \tag{3.19}$$

Final battery and fuel weights for the design range and DOC mission are shown in Table 3.13.

Table 3.13: Battery and fuel specifications for design range and DOC mission - To be updated

	Design range	DOC mission
Battery weight [kg]	4680	4680
Fuel weight [kg]	2315	1568

3.6.4. Mass Breakdown

Table 3.14 contains a top-level mass breakdown for the final aircraft configuration of this project, and Figure 3.10 contains a breakdown with system masses that correspond to this table.

As a result of the hybrid-electric propulsion system architecture, the aircraft is noticeably heavier than similar aircraft, as indicated within Figure 3.8a. Indeed, for conventional aircraft with an operational empty mass of approximately 12 tonnes, the maximum takeoff mass typically hovers around 20 tonnes. In this case, the aircraft is almost 5 tonnes heavier at 24.93 tonnes. This increase in mass is due to the battery mass, and the additional engine mass as a result of the larger power that is required to support this weight. Moreover, it may even be likely that the engine mass is slightly underestimated, as the turboprop rated power was simply taken as the maximum power required from the engine over the mission profile, not accounting for a potential installation penalty that would be encountered. For the purposes of this project, the approach that was taken has been considered sufficient, although the engine power requirement should be investigated in further detail during future stages of this project. Moreover, a battery energy density of 550 Wh/kg is somewhat ambitious for the year 2040, and the maximum takeoff mass would be noticeably increased if this battery specific energy would not be attained.

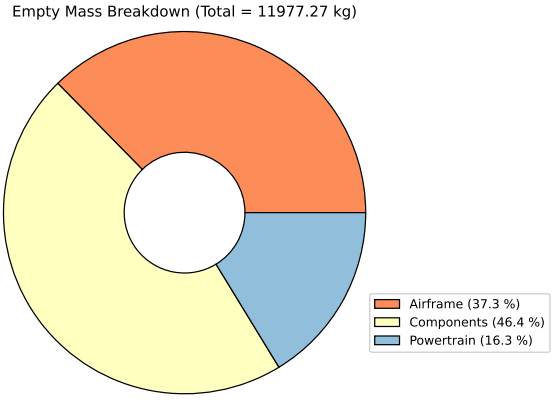

(a) The overall aircraft mass breakdown.

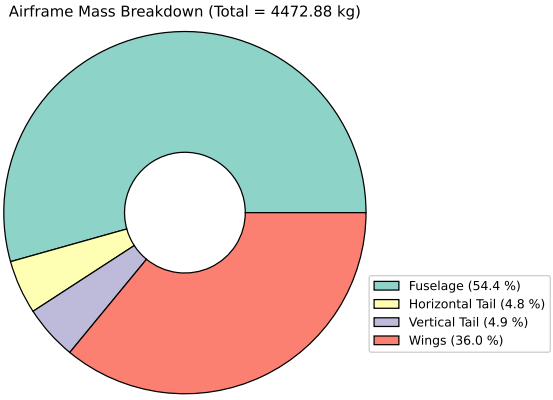

(b) The airframe group mass breakdown.

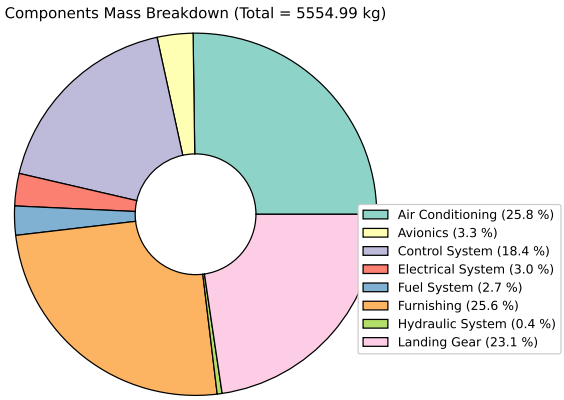

(c) The onboard components group mass breakdown.

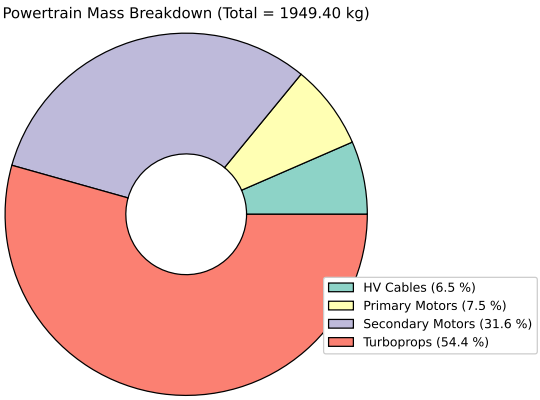

(d) The powertrain group mass breakdown.

Figure 3.10: Plots containing the mass breakdown for the final aircraft configuration (will replace accordingly).

Table 3.14: Top-level breakdown of masses for major groups of the final aircraft configuration.

Major Group	Total Mass (kg)	Fraction of MTOW (%)
Operational Empty Mass	12131.9	48.67
Battery Mass (Total)	4680.05	18.78
Fuel Mass	2315.05	9.287
Maximum Payload	5800.00	23.27
Maximum Takeoff Mass	24927.0	100.0
Maximum Zero Fuel Weight (Including Batteries)	22612.0	90.71
Maximum Zero Fuel Weight (Not Including Batteries)	17931.9	71.94

3.7. Performance

3.7.1. Mission Profile

The mission profile of the aircraft for an 800 km design range, along with a 185 km and 30 minutes holding reserve fuel policy is shown in Figure 3.11. A cruise altitude of 17000 ft was set, stemming from the top level requirement on the time to climb to flight level (FL) 170. A loiter altitude of 6000 ft was chosen to comply with one of the holding altitude groups specified by the FAA [2]. The loiter time of 30 minutes for both the design range and reserve fuel policy comes from the top level requirement of 30 minutes holding for the reserve fuel policy. Lastly, a diversion cruise altitude of 10000 ft was chosen to ensure that the passengers are able to breathe if there is no oxygen left in the cabin [25].

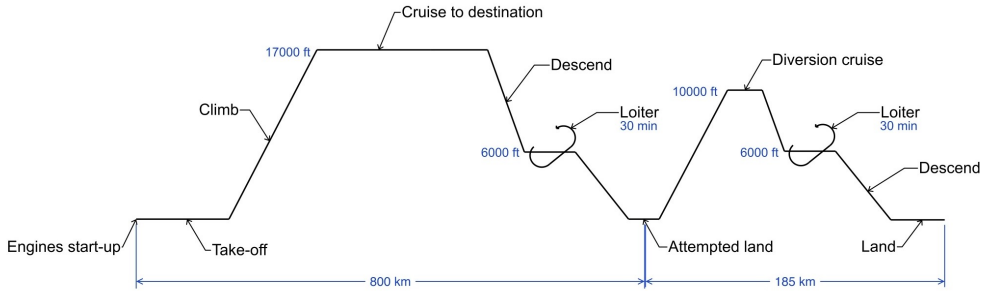

Figure 3.11: Mission for a design range of 800 km and a reserve fuel policy of 185 km with 30 minutes holding (not to scale).

3.7.2. Energy Mission Analysis

The energy mission analysis is used to calculate the energy required for every mission segment defined in the mission profile shown in Figure 3.11. This energy can be further used to find the required fuel weight and battery weight of the aircraft. To find the energy required for every mission segment, the time stepping method proposed by de Vries, et. al. in [45] was applied. This states that the energy for a mission segment can be found through Equation 3.20, where P is the power required for this segment and t is the time it takes to complete the segment. One can then use the supplied power ratio to find the battery energy required and fuel energy required. To find the power required for every mission segment, one can find the force required, F, and the velocity, V, of the aircraft during the segment since $P = F \cdot V$. However, for climb, one can use the power available during climb. The time to climb was calculated by splitting the climb profile into several segments and using Equation 3.21, in which $ROC_{max,i}$ the maximum rate of climb during one segment and dH is the change in altitude. For descent, the required thrust was found for a set of altitudes as thrust, velocity and drag, among other variables change with altitude. Though, sometimes the descent can also be performed as a gliding flight. This is because the weight is larger than the drag and the aircraft therefore does not require any additional force to descend. This means that the power and therefore energy required is zero. For cruise and loiter, the velocity is assumed to be constant when estimating the energy required.

$$\Delta E = P \Delta t \tag{3.20}$$

$$t_{climb} = \sum_{i} \frac{dH}{ROC_{max,i}} \tag{3.21}$$

The energy values for each mission segment corresponding to the chosen hybrid-electric system architecture configuration (Configuration 5), are shown in Table 3.15.

Table 3.15: Total energy required for every mission segment for 800 km design range and 185 km reserve fuel policy

Mission Segment	Energy [MJ]
Taxi out	0.0075
Takeoff	147.2
Climb	5532
Cruise	58803
Descent	4.83
Loiter	12450

Mission Segment	Energy [MJ]
Diversion climb	3105
Diversion cruise	10007
Diversion descent	0
Diversion loiter	11341
Land	0
Taxi in	0.0038

3.7.3. Takeoff and Landing Distance

The takeoff and landing distances were calculated according to the method provided by Ruijgrok [32]. The main purpose of calculating the takeoff and landing distance is to check whether these requirements are met. However, they are also used to estimate the fuel and battery weight required for these mission segments, though their effect is minimal. The takeoff and landing distances were calculated by breaking the distances into a ground and airborne section. The screen height for takeoff and landing is 15.2 m [32]. For takeoff, the ground distance is calculated by integrating velocity divided by acceleration starting from $V = 0$ m/s to the liftoff velocity, V_{LOF}, which is equal to $1.15V_{\text{stall}}$ [32]. The airborne distance is found by finding when the aircraft reaches the screen height. The airborne phase of the landing distance starts when the aircraft is at the screen height. During this phase, the aircraft is flying at a descent angle of 3°, as necessary for the ILS at an airport and the aircraft is flying at an approach velocity of $1.3V_{\text{stall}}$ [32]. The ground distance of the landing phase was obtained by estimating how much distance is required for the aircraft to return to a standstill after touchdown. No thrust reversers are applied during this estimation, as required by the CS-25 regulations. The take-off distance was calculated to be 840 m and the landing distance 860 m.

3.7.4. Performance Diagram

The performance diagram was determined based on Ruijgrok's approach in reference [32]. The available power, P_{a}, was determined through the power loading requirement and the maximum takeoff weight. It is assumed that the P_{a} is constant and provided by the variable-pitch propeller blade. On the other hand, the required power P_{r} was found using drag and flight speed. The difference between P_{a} and P_{r} is the excess power P_{c}. The excess power can increase either the altitude or the forward flight speed [32]. Thus, the maximum ROC can be found for the maximum P_{c}. The maximum ROC is the most important factor for minimising the aircraft's climb time to cruise altitude [32]. Figure 3.12 shows the performance diagram at sea level conditions. The maximum ROC was computed to be 22.54 m/s at a flight speed of 69.14 m/s. The altitude also influences the power requirement, as the air density decreases with increasing altitude. P_{a} decreases with increasing altitude, while P_{r} increases for the same flight speed. Figure 3.13 shows the maximum ROC at different altitudes. Eventually, the maximum ROC reaches zero at the theoretical ceiling altitude, which means no excess power is available. The theoretical ceiling was found to be 11544 m for the final design of this project.

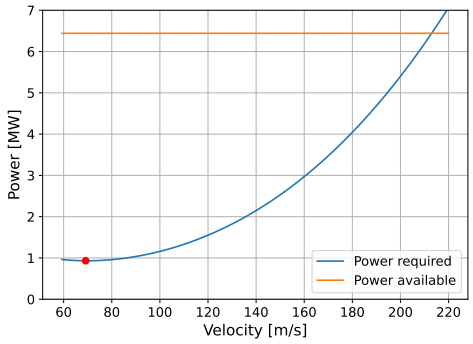

Figure 3.12: Performance diagram at the sea level

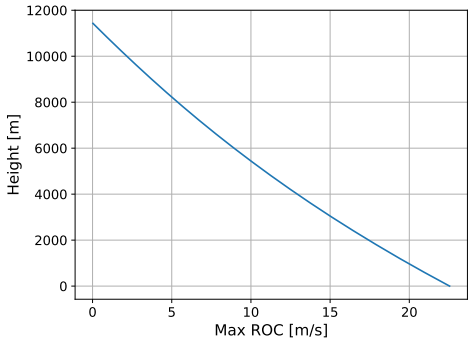

Figure 3.13: Max ROC at the different altitude.

3.7.5. Flight Envelope

Figure 3.14 shows the design flight envelope. The stall speed was plotted as the lower speed limit on the left-hand side. At each altitude, the intersection between the available and required power curves at the minimum speed occurs at a velocity slower than the stall speed. Until at $11392[m]$, the minimum

speed was determined by the power curve intersection. This intersection is taken as the new lower speed limit. On the right-hand side, the intersection of P_a and P_r at a higher speed determines the speed the thrust can sustain. The flight speed at the maximum rate-of-climb was plotted between the stall and thrust limit. The intersection point of the three lines is the theoretical ceiling. At the theoretical ceiling, the P_a and P_r intersect at only one point. At this point, the converged speed is $128.82[m/s]$.

3.7.6. Payload Range

The payload-range diagram was determined through the fuel weight in the different mission segments and the modified Breguet range equation as shown in the Equation 3.22 [46]. Table 3.7 presents the efficiency values applied for the series-parallel powertrain. The payload-range is assumed to be the cruise range [32]. With the fuel weight burned in the different mission segments, the cruise segment's start and end fuel weight was defined. Figure 3.15 shows the payload-range diagram for the design.

$$R = \eta_3 \frac{e_{\mathsf{F}}}{g} \left(\frac{L}{D}\right) \left(\eta_1 + \eta_2 \frac{\Phi}{1-\Phi}\right) \times \ln\left(\frac{W_{\mathsf{OE}} + W_{\mathsf{PL}} + (g/e_{\mathsf{BAT}})\, E_{0,\mathsf{BAT}} + (g/e_{\mathsf{F}})\, E_{\mathsf{F}}\,(t_{\mathsf{start}})}{W_{\mathsf{OE}} + W_{\mathsf{PL}} + (g/e_{\mathsf{BAT}})\, E_{0,\mathsf{BAT}} + (g/e_{\mathsf{F}})\, E_{\mathsf{F}}\,(t_{\mathsf{end}})}\right) \tag{3.22}$$

The design range is indicated by Point B, and is calculated with a maximum fuel and payload weight. It was found to be 1329 km. The maximum range then increases as the payload is replaced by the fuel. Because the fuel tank volume is limited by the maximum fuel tank capacity, the aircraft can only fly to 2026 km at Point C, with the full fuel load. It is noted that the fuel tank length was chosen as $0.3b$ to allow a moderate amount of extra fuel volume. The range can slightly increase to 2586 km at Point D when burning the full fuel load without the payload weight due to the lighter aircraft. The take-off weight eventually decreases when the total usable fuel weight becomes constant.

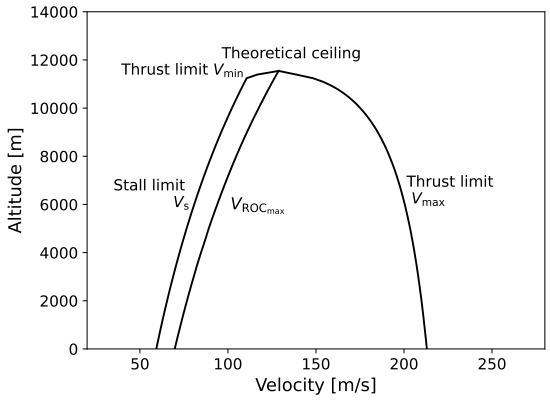

Figure 3.14: Flight envelope of the design

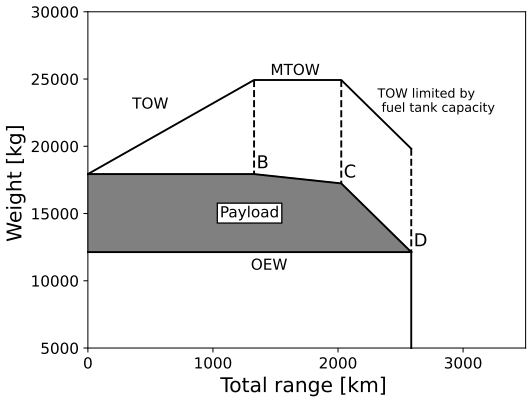

Figure 3.15: Payload range diagram

3.7.7. Emissions

In-Flight Emissions

Because SAF is similar in chemical structure to kerosene, in-flight emissions are not eliminated. SAF emits the same amount of CO_2 per kg as kerosene. Depending on the feedstock used for producing SAF, NO_x emissions may be reduced by as much as 12%. However, this does depend on the amount of impurities present in the fuel [18, 1, 10]. The in-flight emissions are analysed for both a case of where NO_x emissions are the same as kerosene and a case where NO_x emissions are reduced by 12%.

When estimating emissions, it is common to consider the landing/takeoff cycles (LTO) and cruise separately. The LTO cycle considers emissions below an altitude of 1000 m. With an estimated power of 800 shp per engine for the conventional turboprops, 3.16 kg of CO_2 is emitted per kilogram of fuel used in the LTO cycle. Moreover, approximately 0.3 kg of NO_x will be emitted during one LTO cycle, without considering the possible decrease in NO_x with SAF [12]. It is assumed that per mission, two LTO cycles will occur due to the reserve fuel policy that must be accounted for.

For cruise, over 2000 shp must be supplied by each engine because the distributed propulsion system is not being used. This means that 14.2 g of NO_x is emitted per kilogram of fuel used. The emissions per kilogram of fuel being burned during cruise are also 3.16 kg of CO_2 [12].

The estimated emissions and emission breakdown is presented in Table 3.16. Both the emissions for a design range of 800 km with the reserve fuel policy and for the DOC missions with the reserve fuel policy are shown. The total CO_2 LTO emissions for the design range are equal to 238 kg, which includes the trip and reserve LTO emissions. If only considering the trip, the CO_2 LTO emission is 109.7 kg. For the DOC mission, the trip CO_2 LTO emission is 106.3 kg. Both of the missions result in a decrease of more than 100 kg in CO_2 LTO emissions in comparison to other turboprops with a shaft horsepower less than 1000 shp per engine during the LTO cycle [12], meaning more than a 52% decrease in CO_2 LTO emissions. A 12% decrease in LTO NO_x emissions is possible if using a SAF with less impurities, but this cannot be guaranteed as different airports may use different SAFs.

Table 3.16: In-flight emissions for design range and DOC mission

		Design range		DOC Mission	
		No NO_x decrease	12% NO_x decrease	No NO_x decrease	12% NO_x decrease
LTO emissions	CO_2 [kg]	179.2	179.2	173.5	173.5
	NO_x [kg]	0.6	0.468	0.6	0.468
Cruise emissions	CO_2 [kg]	7134	7134	4766	4766
	NO_x [kg]	31.9	28.1	21.3	18.7
Total emissions	CO_2 [kg]	7313	7313	4940	4940
	NO_x [kg]	32.5	28.6	21.9	19.2
For trip	CO_2 [kg]	5581	5581	3102	3012
	NO_x [kg]	24.8	21.8	14.2	12.5
For reserve	CO_2 [kg]	1732	1732	1838	1838
	NO_x [kg]	7.7	6.8	7.7	6.7

Life Cycle Emissions

As can be seen from the in-flight emissions, significant amounts of CO_2 are still being emitted, especially during cruise. However, the main benefit of using SAF is a reduction in life-cycle emissions. This is because SAF closes the carbon loop by recycling carbon through the use of renewable feedstocks [35]. It is estimated that SAF may emit up to 80% less CO_2 than kerosene over its life-cycle and sometimes more, though this value is highly dependent on the type of feedstock that is used [18, 3]. For example, using the Fischer-Tropsch (FT) conversion technology with agricultural residues as the fuel feedstock can save between 89% and 94% in direct emissions when compared to fossil-fuel based aviation fuels [3]. Though, if using the ethanol to jet conversion technology with corn grain as the fuel feedstock, then the decrease in direct emissions is approximately only 26% [3].

An estimation of the fuel production emissions for the design range, assuming no reserve fuel, is compared to a 800 km mission with the ATR42 (no reserve fuel) in Table 3.17. As can be seen, if using a FT conversion technology with agricultural residues, it is possible to reduce the SAF production emissions in comparison to fossil-based aviation fuel. However, if the ethanol to jet conversion technology has been used with corn grain as feedstock, there is not a decrease in the fuel production emissions. While this SAF production method does emit less gCO_2eq per MJ, the high fuel weight required for the hybrid electric configuration causes the higher production emissions. Though, less gCO_2eq are still being emitted compared to if a fossil-based aviation fuel were to be used as the fuel source.

Table 3.17: Comparison of fuel production emissions to ATR42

	Bio-Based Aviation Fuel Pathways	Design range – no reserve fuel	ATR42 800 km mission – estimated
CO_2 eq [tonnes]	Fossil-based aviation fuel	6728	4217
	FT with agricultural residues	740	N/A
	Ethanol to jet conversion technology with corn grain	4980	N/A

3.7.8. Direct operating cost estimation

The direct operating cost has been estimated using the method outlined in reference [23], and verified by comparing the results to [28]. This way, the maintenance and crew costs are estimated. The numbers obtained for these are then corrected for inflation, such that they represent present-day euros. The crew cost is calculated based on the assumption of 2 pilots and 2 flight attendents. The fuel and electricity costs are estimated differently. First, the required fuel and electricity for a 400 km mission are obtained. The electricity price was estimated as 12.54 €/kWh by [15] in 2020. The fuel price was estimated as 1.53 €/kg, using data from [11]. The total cost of fees (landing, air traffic control and ground handling) is estimated using a method from Fokker, provided in [33]. The resulting costs are shown in Table 3.18. They are calculated for the 400 km DOC benchmark mission. It can be seen that fuel represent the highest cost source, followed by fees. Due the short range of the DOC mission,

more cycles are performed per 100 km, explaining the high relative cost of the fees. Fuel costs are high because of the relatively high fuel consumption of the aircraft and the high cost of SAF. Although not considered, this may also attract high carbon taxes, depending on the type of SAF employed. Using more battery power might be a solution, as the cost of electricity is very low. However, this may lead to an unacceptably high weight, and consequently increased fuel consumption. Crew and maintenance cost are both higher than what is estimated for the ATR. It is not clear why this is the case, as the amount of crew is the same. Furthermore, the electric engines were not considered in the cost model. More detailed estimations, including the cost of the electric system should be performed in the future.

Table 3.18: Different costs per 100 km per passenger as calculated for the DOC mission.

	EGRET	ATR-72 (1241 km mission) [23]
Maintenance cost [€/100 pax km]	4.61	1.40
Crew cost [€/100 pax km]	5.91	2.02
Fuel cost [€/100 pax km]	11.9	2.31
Electricity cost [€/100 pax km]	0.44	N/A
Fees [€/100 pax km]	10.1	2.70
Capital [€/100 pax km]	2.75	2.99
Total [€/100 pax km]	35.8	11.4

3.8. Fulfillment of Top-Level Aircraft Requirements

Table 3.19 contains the aircraft's characteristics in comparison to the top-level requirements. It is clear from this that the aircraft satisfies all top-level requirements of this project. The results presented in this table were obtained using the methods outlined within the preceding sections of this report.

Table 3.19: A list of top-level aircraft requirements that have been maintained throughout the course of the project.

TLAR	Calculated Value	Required Value
Design cruise speed	Mach 0.48	$\leq$ Mach 0.48
Rate of Climb (MTOM, SL, ISA)	4437 ft/min (22.54 m/s)	$\geq$ 1850 ft/min (9.398 m/s)
Time required to climb to FL 170	6.5 minutes	$\leq$ 13 minutes
Maximum operating altitude	11392 m (37375 ft)	7620 m (25000 ft)
Maximum take-off field length	840 m	1000 m
Maximum landing field length	860 m	1000 m

The remaining top-level requirements were inputs to the design tools that were used and thus do not need to be verified. In future, more detailed studies should be performed to more precisely characterize the aircraft's take off and landing field lengths (i.e. accounting for hot and high conditions).

4

Conclusions

The purpose of this project was to develop a regional hybrid electric aircraft with an expected entry into service by the year 2040. The aircraft that was developed satisfies all top-level requirements contained within Table 1.1, as imposed by the *FutPrInt 50 Academy*. The reason for developing a hybrid-electric aircraft was to investigate whether it would be possible to decrease the overall environmental impact of the aviation sector, in particular by decreasing carbon emissions.

During the course of this project, subsystem-level trade-offs were performed to determine a suitable propulsion system architecture and primary energy carrier for the aircraft. At this stage, only a qualitative assessment was performed. As a result of these trade-offs, SAF was selected as the primary energy carrier, and the propulsion system architecture was chosen to be a parallel/series partial hybrid (although both the parallel and series propulsion system architectures were not ruled out). After performing the subsystem-level trade-off, an aircraft-level trade-off was performed to determine the final aircraft concept that would be pursued during this project. For this trade-off, three different configurations were evaluated both qualitatively and quantitatively. The outcome of this trade-off was that a narrow-body aircraft with a low-wing and conventional tail configuration was selected, with a series/parallel partial hybrid propulsion system architecture. The primary energy carrier of this configuration is SAF and the secondary energy carrier is batteries. The series propulsion system features distributed propellers and the parallel propulsion system features twin conventional turboprop engines.

After completing the trade-offs,low-fidelity analyses were performed with the chosen configuration to ensure that it satisfies all top-level aircraft requirements. For this step, a dedicated aircraft design tool was developed and tested. The analysis was multidisciplinary, taking into account aerodynamics, structures, propulsion and power, stability and control and performance. The distributed propulsion system was designed such that the electric motors provided most of the power at take-off, climb and landing, such that emissions near the ground were minimised. During cruise, the aircraft only uses the conventional propulsion system. The electrical propulsion required relatively heavy batteries, which caused significant increases in overall fuel consumption and emissions. This is something that should be addressed in further design stages, to prevent high operating costs and harming the environment. A possible solution would be to reduce the shaft power ratio during climb, and only use the electric motors at take-off and landing, where their lift-augmentation capabilities could allow the use of a smaller wing, and thus lower weight.

The aircraft has a maximum take-off mass of 24926 kg, consuming 1567 kg of fuel and 709 kWh of electrical energy for a 400 km mission. When including maintenance, fees, crew cost and capital cost, the aircraft costs 35.8 €/100 pax km to operate. This is much more than estimated for the ATR72 [23]. Most of the cost comes from fuel, indicating an important area for optimisation.

References

[1] 4Air. *Sustainable Aviation Fuel - An Introduction*. Sustainability solutions program dedicated to private aviation.

[2] Federal Aviation Administration. *ENR 1.5 Holding, Approach, and Departure Procedures*. FAA procedures. URL: https://www.faa.gov/air_traffic/publications/atpubs/aip_html/part2_enr_section_1.5.html.

[3] European Union Aviation Safety Agency. *Sustainable Aviation Fuel Overview*. URL: https://www.easa.europa.eu/eaer/topics/sustainable-aviation-fuels/sustainable-aviation-fuel-overview.

[4] L. Ahlgren. *Could Ammonia Be The Solution To Aviation's Clean Propulsion Needs?* Sept. 2022. URL: https://simpleflying.com/ammonia-clean-aircraft-fuel/.

[5] Airbus. *Airbus' high-voltage battery technology prepares for EcoPulse flight test and beyond*. Mar. 2022. URL: https://www.airbus.com/en/newsroom/news/2022-03-airbus-high-voltage-battery-technology-prepares-for-ecopulse-flight-test.

[6] R. Babikian, S. Lukachko, and I. Waitz. "The historical fuel efficiency characteristics of regional aircraft from technological, operational, and cost perspectives". In: *Journal of Air Transport Management* 8.6 (2002), pp. 389–400. ISSN: 0969-6997. DOI: 10.1016/S0969-6997(02)00020-0.

[7] Battery 2030+. *Inventing the Sustainable Batteries of the Future: Research Needs and Future Actions*. en. Research organization documentation of research areas and goals. Feb. 2022. URL: https://battery2030.eu/research/roadmap/ (visited on 09/02/2022).

[8] Battery University. *BU-808: How to Prolong Lithium-based Batteries*. en. Nov. 2021. URL: https://batteryuniversity.com/article/bu-808-how-to-prolong-lithium-based-batteries (visited on 09/02/2022).

[9] R. C. Boehm et al. "Lower heating value of jet fuel from hydrocarbon class concentration data and thermo-chemical reference data: An uncertainty quantification". In: *Fuel* 311 (2022). ISSN: 0016-2361. DOI: 10.1016/j.fuel.2021.122542.

[10] M. Braun-Unkhoff, U. Riedel, and C. Wahl. "About the emissions of alternative jet fuels". In: *CEAS Aeronautical Journal* 8 (2017). DOI: 10.1007/s13272-016-0230-3.

[11] Rafael S. Capaz et al. "Mitigating carbon emissions through sustainable aviation fuels: costs and potential". In: *Biofuels, Bioproducts and Biorefining* 15.2 (Mar. 2020), pp. 502–524. ISSN: 1932-104X. DOI: 10.1002/BBB.2168. URL: https://repository.tudelft.nl/islandora/object/uuid%5C%3A95cd214d-7923-4c22-93e8-6b40d80022fe.

[12] The Intergovernmental Panel on Climate Change. *Mobile Combustion*. 2006 IPCC Guidelines for National Greenhouse Gas Inventories. 2019.

[13] Southwest Electronic Energy Corp. *Lithium-Ion Information Guide*. 2021. URL: https://www.swe.com/lithiumion/.

[14] I. Coutts. *Turnaround: Here's What Happens When An Aircraft Is On The Ground*. June 2022. URL: https://simpleflying.com/aircraft-turnaround-process/.

[15] *Electricity Prices in Europe - Who pays the most? [2010 - 2021]*. 2021. URL: https://strom-report.de/electricity-prices-europe/ (visited on 08/30/2022).

[16] Committee Emissions et al. *Commercial aircraft propulsion and energy systems research: Reducing global carbon emissions*. Sept. 2016, pp. 1–122. DOI: 10.17226/23490.

[17] S. J. Gerssen-Gondelach and A. P.C. Faaij. "Performance of Batteries for Electric Vehicles on Short and Longer Term". en. In: *Journal of Power Sources* 212 (May 2012), pp. 111–129. ISSN: 0378-7753. DOI: 10.1016/j.jpowsour.2012.03.085. (Visited on 09/02/2022).

[18] Air Transport Action Group. *Beginner's Guide to Sustainable Aviation Fuel*. 2017.

[19] S. Gudmundsson. “Chapter 6 - Aircraft Weight Analysis”. In: *General Aviation Aircraft Design*. Ed. by S. Gudmundsson. Boston, Massachusetts, USA: Butterworth-Heinemann, 2014, pp. 133–180. ISBN: 978-0-12-397308-5. DOI: 10.1016/B978-0-12-397308-5.00006-4.

[20] B. Khaki and P. Das. “Sizing and Placement of Battery Energy Storage Systems and Wind Turbines by Minimizing Costs and System Losses”. In: (Mar. 2019).

[21] N. S. López, A. M. Santamaría, and S. G. Castro. “Preliminary aerodynamic design and load calculation of a long-range eVTOL aircraft”. en. In: *AIAA SCITECH 2022 Forum*. San Diego, CA & Virtual: American Institute of Aeronautics and Astronautics, Jan. 2022. DOI: 10.2514/6.2022-1331. (Visited on 08/08/2022).

[22] L.M. Nicolai and G. Carichner. *Fundamentals of Aircraft and Airship Design*. AIAA education series v. 1. American Institute of Aeronautics and Astronautics, 2010. ISBN: 978-1-60086-751-4.

[23] Mihaela Florentina Niță and Dieter Scholz. “Aircraft Design Studies Based on the ATR 72”. In: (June 2008).

[24] F. Oliviero. *Requirement Anaysis and Design Principles for Aircraft Stability and Control*. University Lecture. 2021.

[25] International Civil Aviation Organization. *Extended Diversion Time Operations Manual*. ICAO guidelines. 2014.

[26] T. Placke et al. “Lithium ion, lithium metal, and alternative rechargeable battery technologies: the odyssey for high energy density”. In: *Journal of Solid State Electrochemistry* 21 (2017), pp. 1939–1964. DOI: 10.1007/s10008-017-3610-7. URL: https://link.springer.com/content/pdf/10.1007/s10008-017-3610-7.pdf.

[27] *Pratt & Whitney Canada Successfully Conducts 100% SAF Flight Test with PW127M Engines Powering Braathens’ ATR Aircraft*. type: Web page. URL: https://www.pwc.ca/en/company/news-and-events/news-details/pratt-whitney-canada-successfully-conducts-10?id=123594 (visited on 08/31/2022).

[28] D. P. Raymer. *Aircraft Design: A Conceptual Approach*. American Institute of Aeronautics, 2012.

[29] M. A. Rendon et al. “Aircraft Hybrid-Electric Propulsion: Development Trends, Challenges and Opportunities”. In: *Journal of Control, Automation and Electrical Systems* 32.5 (2021). ISSN: 21953899. DOI: 10.1007/s40313-021-00740-x.

[30] J. Roskam. *Airplane Design - Part VI: Preliminary Calculation of Aerodynamic, Thrust ans Power Characteristics*. 2004, p. 550. ISBN: 1884885527.

[31] J. Roskam. *Part V: Component Weight Estimation*. 2018, p. 227. ISBN: 978-1-884885-50-1.

[32] J.J. Ruijgrok. *Elements of Airplane Performance*. 2nd ed. Delft, the Netherlands: Delft Academic Press, 2013.

[33] Scholz. “14 Design Evaluation / DOC”. In: (), pp. 1–32.

[34] Singh, S. *How SAF Can Become Cost Competitive Against Conventional Fuel*. en. Apr. 2022. URL: https://simpleflying.com/saf-cost-competitive-jet-fuel/ (visited on 09/02/2022).

[35] SkyNRG. *Sustainable aviation fuel*. en. URL: https://skynrg.com/sustainable-aviation-fuel/ (visited on 09/02/2022).

[36] Power Sonic. *What is a Battery C Rating*. 2021. URL: https://www.power-sonic.com/blog/what-is-a-battery-c-rating/.

[37] Sourmey, I. *Lithium-ion batteries in use: 5 more tips for a longer lifespan*. en. Jan. 2022. URL: https://www.saftbatteries.com/energizing-iot/lithium-ion-batteries-use-5-more-tips-longer-lifespan (visited on 09/02/2022).

[38] *SPM242 Platform | Electric Motor | Helix UK*. URL: https://ehelix.com/products/spm242-electric-motor/ (visited on 09/01/2022).

[39] S. Stückl. “Methods for the Design and Evaluation of Future Aircraft Concepts Utilizing Electric Propulsion Systems”. In: (June 2015).

[40] E. Torenbeek. *Advanced aircraft design: conceptual design, analysis, and optimization of subsonic civil airplanes*. Chichester, West Sussex, United Kingdom: John Wiley & Sons Inc, 2013. ISBN: 978-1-118-56811-8.

[41] E. Torenbeek. *Synthesis of subsonic airplane design: an introduction to the preliminary design, of subsonic general aviation and transport aircraft, with emphasis on layout, aerodynamic design, propulsion, and performance*. Delft : The Hague : Hingham, MA: Delft University Press, 1982. ISBN: 978-90-247-2724-7.

[42] United States Department of Labor. *Ammonia Refrigeration*. en. URL: https://www.osha.gov/ammonia-refrigeration (visited on 09/02/2022).

[43] R. Vos, J. A. Melkert, and B. T. C. Zandbergen. *Aerospace Systems Engineering Elements I: Wing Positioning, Landing Gear and Empennage Design*. University Lecture. 2019.

[44] R. de Vries. "Hybrid-Electric Aircraft with Over-the-Wing Distributed Propulsion Aerodynamic Performance and Conceptual Design". In: (2022). DOI: DOI10.4233/uuid:ef87dc11-e7b2-4726-a41f-28588d64c58d.

[45] R. de Vries, M. T. Brown, and R. Vos. "A preliminary sizing method for hybrid-electric aircraft including aero-propulsive interaction effects". en. In: *2018 Aviation Technology, Integration, and Operations Conference*. Delft, The Netherlands: American Institute of Aeronautics and Astronautics, June 2018. DOI: 10.2514/6.2018-4228. (Visited on 09/02/2022).

[46] R. de Vries, M. F. M. Hoogreef, and R. Vos. "Range Equation for Hybrid-Electric Aircraft with Constant Power Split". en. In: *Journal of Aircraft* 57.3 (May 2020), pp. 552–557. ISSN: 1533-3868. DOI: 10.2514/1.C035734. URL: https://arc.aiaa.org/doi/10.2514/1.C035734 (visited on 07/17/2022).

[47] Whalen, C. *Use ammonia for shipping, synthetic hydrocarbons for aviation*. en. Dec. 2021. URL: https://www.carboncommentary.com/blog/2021/12/1/use-ammonia-for-shipping-synthetic-hydrocarbons-for-aviation (visited on 09/02/2022).

[48] Willcox, K. *16.885 Aircraft Systems Engineering Cost Analysis*. en. Sept. 2002. URL: https://dspace.mit.edu/bitstream/handle/1721.1/36378/16-885JFall2003/NR/rdonlyres/Aeronautics-and-Astronautics/16-885JFall2003/8CACE2FE-A136-4B03-93B6-08F81FC911BB/0/pres_willcox.pdf (visited on 09/02/2022).

[49] Willuhn, M. *Affordable hydrogen-fueled flight possible in 2035*. en. June 2020. URL: https://www.pv-magazine.com/2020/06/24/affordable-hydrogen-fueled-flight-possible-in-2035/ (visited on 09/02/2022).

[50] J. Zamboni et al. "A Method for the Conceptual Design of Hybrid Electric Aircraft". en. In: *AIAA SCITECH 2019 Forum*. San Diego, California, USA: American Institute of Aeronautics and Astronautics, Jan. 2019. DOI: 10.2514/6.2019-1587. (Visited on 09/02/2022).

A

Three-View Drawings

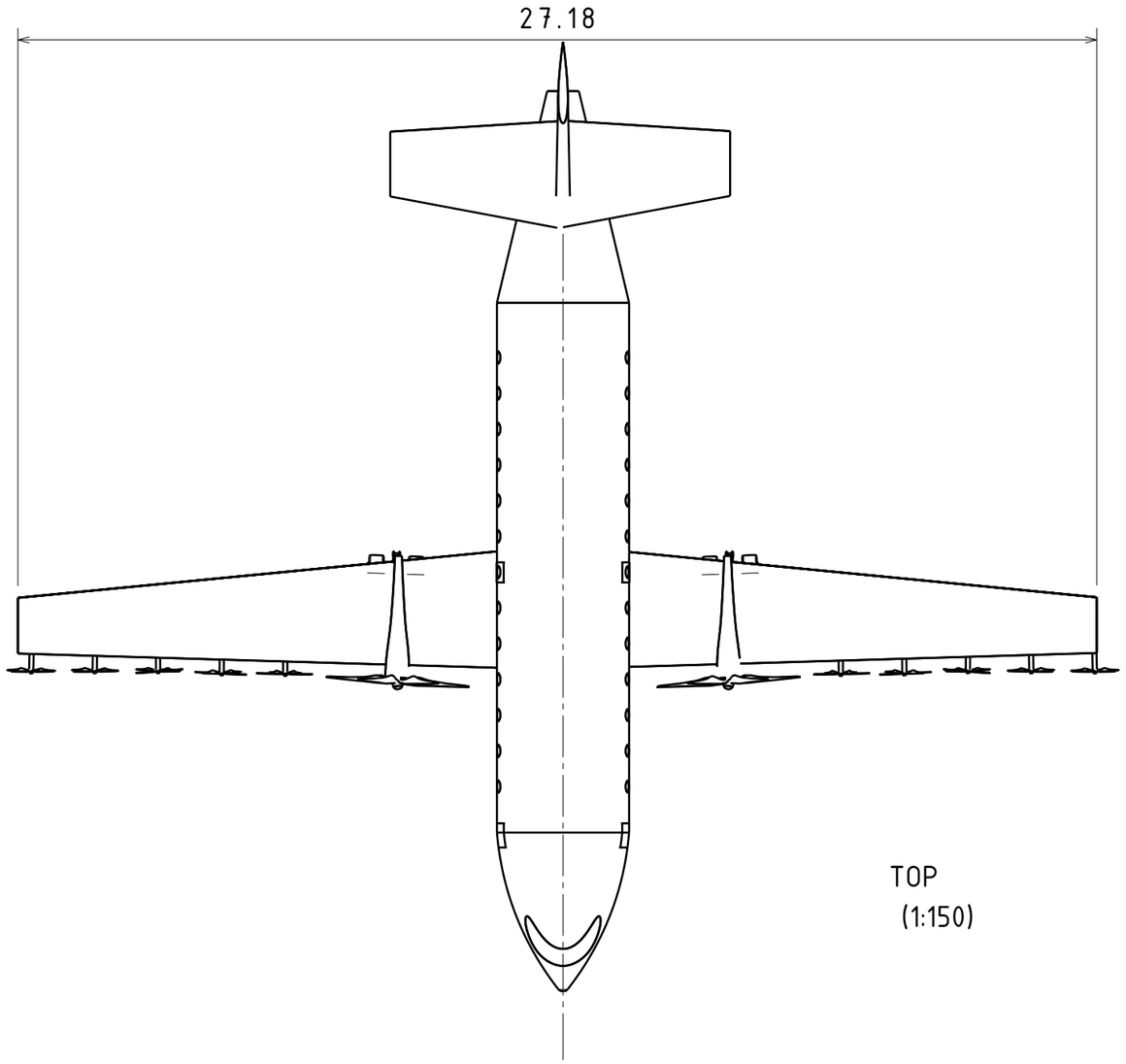

TOP
(1:150)

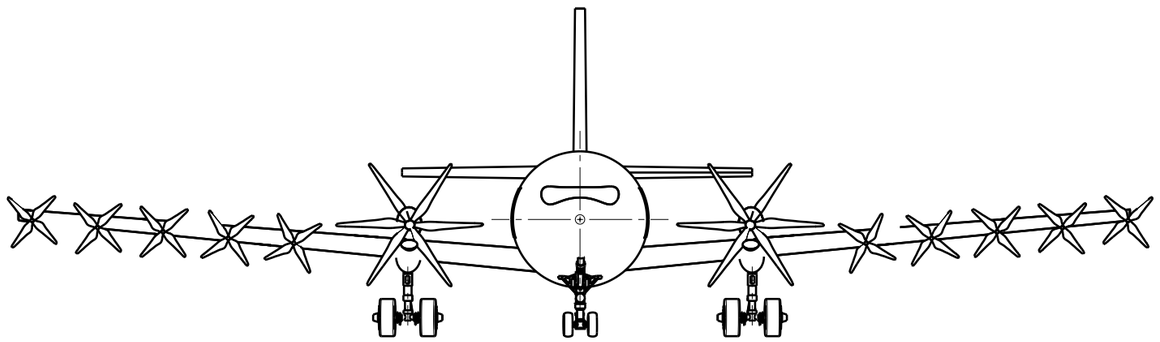

FRONT
(1:150)

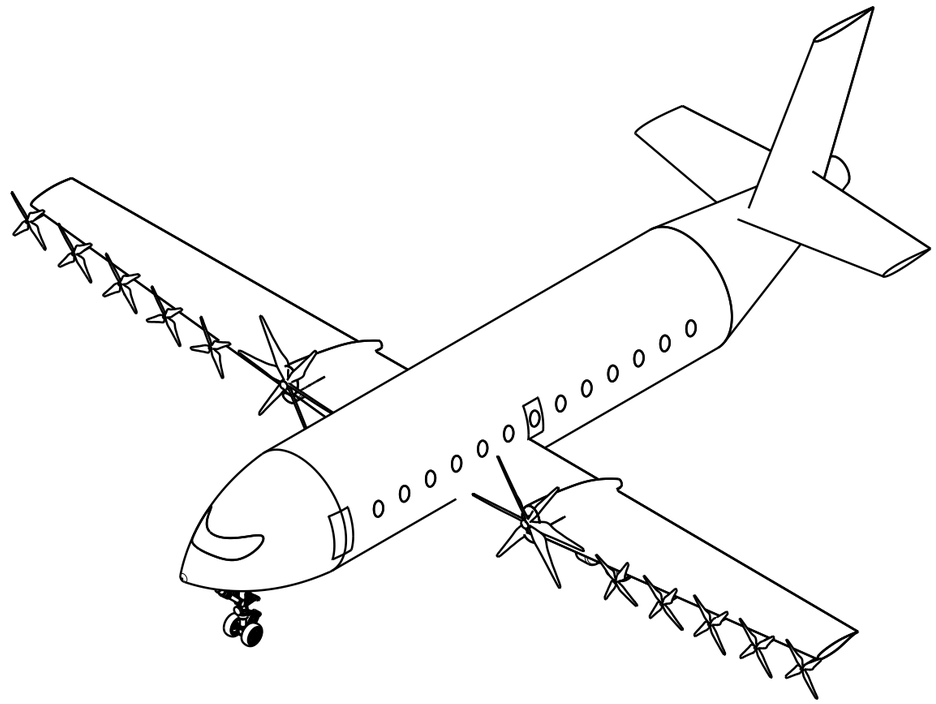

ISOMETRIC
(1:150)

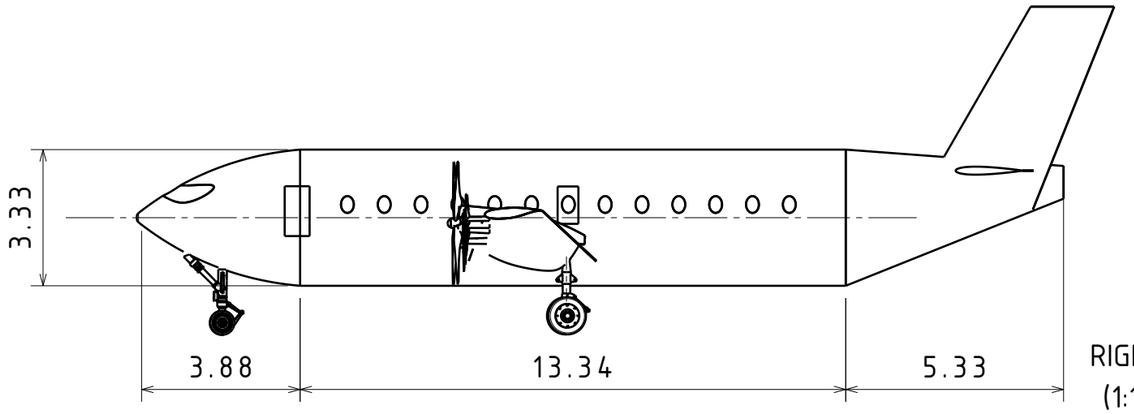

RIGHT
(1:150)

DASSAULT SYSTEMES

DRAWN BY: Katarina	DATE: 02/09/2022	DRAWING TITLE: EGRET		
CHECKED BY: XXX	DATE: XXX	SIZE: A3	DRAWING NUMBER: XXX	REV: X
DESIGNED BY: EGRET Team	DATE: 02/09/2022	SCALE: 1:150	WEIGHT(kg): XXX	SHEET: 1/1